6-2022

Performance Study of Post-processed Additively Manufactured Low Thrust Nozzles

Tyler W. Gerhold

PERFORMANCE STUDY OF POST-PROCESSED ADDITIVELY MANUFACTURED LOW THRUST NOZZLES

THESIS

Tyler W. Gerhold, Civilian, USAF

AFIT-ENY-MS-22-J-074

DEPARTMENT OF THE AIR FORCE
AIR UNIVERSITY

AIR FORCE INSTITUTE OF TECHNOLOGY

Wright-Patterson Air Force Base, Ohio

AFIT-ENY-MS-22-J-074

PERFORMANCE STUDY OF POST-PROCESSED ADDITIVELY MANUFACTURED LOW THRUST NOZZLES

THESIS

Presented to the Faculty

Department of Aeronautics and Astronautics

Graduate School of Engineering and Management

Air Force Institute of Technology

Air University

Air Education and Training Command

In Partial Fulfillment of the Requirements for the

Degree of Master of Science in Astronautical Engineering

Tyler W. Gerhold, B.S.

Civilian, USAF

June 2022

AFIT-ENY-MS-22-J-074

PERFORMANCE STUDY OF POST-PROCESSED ADDITIVELY MANUFACTURED LOW THRUST NOZZLES

Tyler W. Gerhold, B.S.

Civilian, USAF

Committee Membership:

Dr. Carl Hartsfield
Chair

Dr. Mark Reeder
Member

Dr. Fred Schauer
Member

AFIT-ENY-MS-22-J-074

Abstract

This research explores metal post-processing techniques to effectively reduce the large anomalous protrusions found in small additively manufactured low thrust rocket nozzles. Research has found that nozzles of this kind can experience losses in thrust of over 40%. Analytic theory of adiabatic nozzle flow with viscous losses for additively manufactured nozzles does not align with what has been found when tested experimentally. Compressible flow losses, such as shock wave formation inside the nozzle diverging cone, are likely the leading causes of such loss. Reduction in nozzle irregularities can likely yield results seen in analytic theory with similar performance to traditional subtractive manufacturing methods for low thrust nozzle design. Methods such as abrasive flow machining, electro-polishing, milling, wire EDM skimming, and high-temperature coatings are investigated and tested experimentally to compare laboratory results to analytic theory and traditionally manufactured low thrust nozzles. Nozzle performance increases showed to be greater than 20% across various explored post-processing techniques.

Acknowledgments

I would like to express my sincere appreciation to my faculty advisor, Dr. Carl Hartsfield, for his guidance and support throughout the course of this thesis effort and for helping me determine an experimental topic that could be done while being a part-time student. The insight and experience were certainly appreciated. I would, also, like to thank the AFIT Model and Fabrication shop for their fantastic and expedited effort to complete component manufacturing.

I would also like to thank my parents for their support in all my endeavors. I would not have been able to accomplish what I have today without the lessons they taught me about hard work and determination to achieve one's goals in life. Thank you.

Tyler W. Gerhold

Table of Contents

Page

List of Figures

Page

List of Tables

Page

List of Symbols

F	Thrust Force
C_F	Thrust Coefficient
$\dot{m}$	Mass Flow Rate
v_2	Exhaust Velocity
p_2	Exit Pressure
p_3	Ambient Pressure
A_2	Exit Area
p_1	Chamber, Nozzle Inlet Pressure
ε	Expansion, Area Ratio
A_t	Throat Area
γ	Ratio of Specific Heats
Re_t	Throat Reynolds Number
ρ	Density
μ	Dynamic Viscosity
d_t	Throat Diameter
v_t	Throat Velocity
T	Temperature
R_a	Average Surface Roughness
f	Fanning Friction Factor
M	Mach Number
ϵ	Absolute Roughness

D_H	Hydraulic Diameter
P_{ell}	Perimeter of Ellipse
A_{ell}	Area of Ellipse
a	Semi-Major Axis of Ellipse
b	Semi-Minor Axis of Ellipse
Q	Volumetric Flow Rate
k	Sand Grain Roughness

Nomenclature

EDM	Electrical Discharge Machining
DMLS	Direct Metal Laser Sintering
LPBF	Laser Powder Bed Fusion
CFD	Computational Fluid Dynamics
LSM	Laser Scanning Microscope
IN718	Inconel 718
AFM	Abrasive Flow Machining
ECP	Electro-polishing
AP	As Printed
ODE	Ordinary Differential Equation
NPT	National Pipe Threaded
CAD	Computer-Aided Design
NPT	National Pipe Thread

PERFORMANCE STUDY OF POST-PROCESSED ADDITIVELY MANUFACTURED LOW THRUST NOZZLES

I. Introduction

1.1 General Issue

Small satellite capability has grown vastly over the last decade. Rideshare opportunities in the space industry have made it feasible for smaller organizations to get their payload to orbit. Since the turn of the millennium, the number of satellite missions has been increasing year over year, each with different goals [1]. Larger satellites in space rely on reaction control thrusters for orbit and attitude maintenance [2]. These systems can be extremely reliable for delivering the satellite's payload to the desired location. Unfortunately, these thruster systems can be difficult to scale down to small satellites that are on the order of centimeters. Machining very small converging-diverging rocket nozzles can be difficult and costly. The rise of additive manufacturing has given the aerospace industry the ability to create small thrusters at a low cost. However, additive manufacture of metals can lead to a much higher surface roughness when compared to traditional machining practices, with estimated sand grain roughness on the order of 30x that of drawn tubing [3]. Because of the scale of the nozzles, the induced viscous forces, due to roughness, largely outweigh the momentum forces of the flow. Viscous effects, drag, and shock waves were found to be the leading causes in loss of thrust coefficient in additively manufactured nozzles [4]. The motivation of this research is to gain a better understanding of the

effects of metal post-processing techniques on additively manufactured rocket nozzle performance for small satellite operations.

1.2 Problem Statement

In a previous study, Tommila found that roughness measurements using a laser scanning microscope showed that the average roughness of both printed and electrical discharge machining (EDM) machined nozzle varieties were nearly the same although the maximum roughness height of anomalous protrusions in the laser powder bed fusion (LPBF) nozzles was significantly higher than the maximum height of irregularities in the machined nozzles [3]. To further understand the impacts of these larger protrusions a CFD study was conducted to quantify the effects of a 100-micron hemispherical protrusion placed in the diverging section of the nozzle near the throat. In the computational fluid dynamics (CFD) study, it was found that the added defect contributed to the formation of multiple complex flow features within the nozzle [4]. Both shock and expansion waves were formed contributing to a decrease in the total pressure within the nozzle, driving a decrease in thrust and therefore thrust coefficient [4]. The goal of this research is to eliminate the shock-inducing protrusions to achieve a nozzle performance close to the previously created analytic model, still including the unavoidable small nozzle viscous effects, and to identify relationships between thrust coefficients and different area ratios with varying Reynolds numbers. This will be explored through various metal polishing processes done to the throat and diverging sections of the nozzle.

1.3 Research Objectives

The following research objectives were determined to further evaluate the suitability of small additively manufactured rocket nozzles for small satellite space application.

1. Redesign low thrust nozzle for upright printing during the LPBF process.
2. Experimentally measure thrust and stagnation pressure of post-processed and "As Printed" (AP) additively manufactured nozzles with controlled mass flow.
3. Calculate thrust coefficients of post-processed and AP additively manufactured nozzles.
4. Compare thrust coefficients of post-processed and AP additively manufactured nozzle designs.
5. Compare the thrust coefficients between all explored post-processing techniques.
6. Compare the thrust coefficients of post-processed additively manufactured nozzles to a quasi-one-dimensional adiabatic compressible flow analytical model with viscous losses.

1.4 Research Focus

The primary focus of this research is to determine whether post-processing the inside of the throat and diverging section of the nozzle is effective in terms of minimizing compressible flow losses caused by large surface protrusions inside this section of the nozzle. Five different techniques including wire EDM, electro-polishing, abrasive flow machining, milling, and inert coating, are explored to determine which process can yield the best results and what is deemed most practical for real-world applications.

1.5 Methodology

The approach to this research is derived from Captain Christopher Tommila's work on low thrust rocket nozzle performance. Rocket nozzles were 3D printed from the nickel-based superalloy Inconel 718, a high-temperature alloy commonly used in rocket engine design and testing. Findings from previous research led to the redesign of the

nozzles. For this research, all nozzles were designed to a 0.508 mm (0.02”) throat diameter. Three different expansion ratios were selected for testing to further explore the relationship of thrust coefficient loss to expansion ratio. The expansion ratios were selected based on previous NASA research and are 10, 20, and 40. Three different Reynolds numbers were selected for testing: 2,500, 5,000, and 10,000. This range of Reynolds numbers was selected and then compared to the outputs from an analytic model for effects comparison. Four to five nozzles were tested for each expansion for each post-processing technique at the three different Reynolds numbers. Five nozzles for each selected expansion ratio were also tested at the varying Reynolds numbers without any post-processing. This allows for comparison of performance metrics of the post-processed nozzles to as printed (AP) nozzles.

Each rocket nozzle test was conducted in a vacuum chamber with starting pressures on the order of 26.7 Pa (0.2 Torr). Before testing, the nozzles were measured, and the hydraulic diameter was determined using a stereomicroscope. Nitrogen gas was heated to a temperature of 600 K and the volumetric flow rate was varied to achieve the desired throat Reynolds numbers. Measurements of thrust, stagnation pressure, and vacuum chamber pressure were taken during each test run.

1.6 Assumptions and Limitations

This research is primarily focused on the overall performance of the designed nozzles. The heat transfer experienced during a run is only a part of the loss mechanisms and not the driving force of this research. It has been found that heat transfer of the gas through the walls of the nozzle does influence performance [5]. For low propellant flow

rates, heat transfer losses can be a significant portion of the total thermal energy available for conversion to kinetic energy [5].

This research was limited by the power supply and capability of the heaters used for maintaining temperature during testing. This research was also limited by the selected 0.508 mm (0.02”) throat diameter. This diameter was selected to maintain the desired low throat Reynolds numbers throughout the experiment. This selection limited the electro-polishing technique electrode from entering the internal channel and instead had to be run without the electrode entering the channel. This process and its limitation will be explained in further detail in Chapter II and IV.

1.7 Preview

Chapter I serves as a preview into the chapters that follow. Chapter II will lay out the literature review, which will consist of the fundamental equations this research is built upon. It will also define the engineering concepts that were considered throughout the course of this research such as low Reynolds number flow, compressible flow losses, additively manufactured part surface roughness, and the proposed post-processing techniques for small additively manufactured rocket nozzles. Chapter III will explain the methodology of the research including the processes and procedures of the experimental setup and testing. Chapter IV includes the results of the execution of the processes and procedures explained in Chapter III and the analysis of the processed data that was collected. Finally, Chapter V will note key findings and summarize the conclusions of the performance impacts on post-processed additively manufactured low thrust rocket nozzles.

II. Literature Review

The purpose of this chapter is to outline the research and theory that supports the experimental testing done on post-processed low thrust micro-nozzles. A review of the ideal rocket and its limitations, as well as viscous and compressible flow losses for low Reynolds number flow, are necessary to lay out the foundation of this research. The equations of an ideal rocket are used to explain the behavior of propulsive devices whose momentum forces largely outweigh their viscous forces. Due to the scale, design, and application of the thrusters designed for this research, they do not obey all the assumptions included in the analysis of an ideal rocket. The Low Reynolds number flow in this experiment is controlled by the mass flow of the gas at the throat of the converging-diverging nozzle. At low Reynolds numbers, viscous forces such as friction and drag dominate the momentum forces of the flow. Minimizing the viscous forces and compressible flow losses is necessary for creating the conditions where the nozzles can perform near their theoretical performance

2.1 Equations of an Ideal Rocket

A rocket functions as an impulsive device. The propulsive force or thrust that a vehicle experiences is obtained by ejecting propellant at high velocity [6]. The thermal potential energy in the selected propellant is transformed into kinetic energy inside the nozzle. This transformation of energy inside the nozzle results in the momentum thrust, which is represented by the product of the propellant mass flow rate and its exhaust velocity [6]. The second term represents the pressure thrust consisting of the product of the nozzle exit area and the difference between the gas exit pressure and the ambient

pressure. The definition of thrust is shown in Equation 1 with the two previously described terms, the momentum and pressure thrust.

$$F = \dot{m}v_2 + (p_2 - p_3)A_2 \tag{1}$$

When a rocket is operating in the vacuum of space or a test chamber with similar conditions, the ambient pressure p_3, is equal to zero so the equation is then reduced to Equation 2 as shown below [6].

$$F = \dot{m}v_2 + p_2A_2 \tag{2}$$

A supersonic nozzle or De Laval nozzle, named after the inventor Gustaf De Laval, is a nozzle consisting of a converging section leading to a minimum area followed by a diverging section [6]. This minimum area portion of the nozzle is commonly referred to as the throat and is where the flow transitions from subsonic to supersonic. The supersonic nozzle design is the only one of interest for rocket propulsion systems as they achieve a high conversion of enthalpy to kinetic energy [6]. Equation 3 shows the expansion or area ratio which is the ratio of the nozzle exit area divided by the nozzle throat area [6].

$$\varepsilon = \frac{A_2}{A_t} \tag{3}$$

Now having definitions for thrust, the different area ratios, and pressures throughout a converging-diverging nozzle, a dimensionless quantity known as thrust coefficient can be derived. This key performance metric can be used for determining the nozzle's effectiveness at creating thrust. The thrust coefficient is written in two different forms. Equation 4 is a useful relationship that can be used for simplifying experimental calculations by obtaining a few easily measurable quantities [6].

$$C_F = \frac{F}{A_t p_1} \tag{4}$$

The thrust coefficient can also be expressed in terms of the ratio of specific heats of the working gas, the nozzle area ratio, and the pressure ratio across the nozzle as seen in Equation 5 [6].

$$C_F = \sqrt{\frac{2\gamma^2}{\gamma-1}\left(\frac{2}{\gamma+1}\right)^{\frac{\gamma+1}{\gamma-1}}\left[1-\left(\frac{p_2}{p_1}\right)^{\frac{\gamma-1}{\gamma}}\right]} + \frac{p_2 - p_3}{p_1}\frac{A_2}{A_t} \tag{5}$$

Although these equations are effective for large rocket engines there are many underlying assumptions that must be evaluated and considered when applying these principles to a smaller scale. Micro-nozzles operating at low Reynolds numbers abide by some of the assumptions contained in these equations but not all. To conduct a complete analysis of low thrust nozzles, an understanding of the limiting assumptions is necessary. The assumptions of the ideal rocket equations at issue are [6]:

1. There is no heat transfer across any gas-enclosed walls, therefore the flow is adiabatic.
2. There is no appreciable wall friction, and all boundary layer effects may be neglected.
3. There are no shock waves or other discontinuities within the nozzle flow.

Given the conditions of micro-nozzle flow, these assumptions are not necessarily valid. The heat transfer effects were studied by Spisz in a NASA low thrust nozzle study. He concluded that at low mass flow rates, heat transfer losses were responsible for a significant reduction in flow kinetic energy [5]. When a nozzle's inner wall has a flow obstruction or a wall protrusion the gas kinetic energy is locally converted back into thermal energy, recovering the stagnation temperature and some pressure in the chamber [6]. In high-temperature rocket engines, this phenomenon can cause localized overheating

and can cause the entire nozzle wall to fail [6]. This localized overheating, even in smaller rocket nozzles, could lead to greater heat transfer loss throughout the system. This research will utilize a very similar experimental setup to that of Tommila and will ignore any potential heat transfer losses experienced during the test, thus the assumption of adiabatic flow [3].

The assumption of no appreciable wall friction can be deemed invalid for additively manufactured nozzles when operating at low Reynolds numbers. This assumption is reasonable for larger rocket designs because any effects due to wall friction are rather small with respect to the nozzle flow conditions. In low Reynolds number micro-thrusters however, any amount of friction along the walls can greatly impact the performance of the nozzle because of its induced effects on nozzle flow behavior [5].

Spisz also found that boundary layer effects can account for a large portion of the nozzle flow area and because of these boundary layer effects, introduce viscous losses that alter the free-stream conditions [5]. In a subsequent study conducted at NASA's Lewis Research Center, Grisnik found through experimentation that large boundary layers filled the exit plane of four different nozzle configurations tested at varying Reynolds numbers [7]. These thick boundary layers were found to be contributing to viscous losses inside the supersonic portion of the nozzle and affecting the flow core density which in turn decreased flow velocity [8].

The presence of shock waves inside these thrusters is known. Tommila researched the effects of surface roughness on nozzle performance and found that the average surface roughness of the LPBF nozzles was quite similar to the traditionally machined nozzles [3]. He also found there to be large protrusions scattered throughout the internal

channel of the thruster with heights much larger than the average surface roughness when the nozzles were sectioned and examined [3]. These protrusions have the potential to be present and scattered in all similarly designed nozzles. In a follow-on study to Tommila's work, a greater examination of these large protrusions was done using a CFD model which proved that a large protrusion near the throat would create shock waves inside the nozzle [4].

These fundamental assumptions incorporated in the ideal rocket equations prove to be controversial when assessing micro-nozzle performance. Wall friction, boundary layer effects, and shock wave formation discussed in this section are very closely related and will be explored in greater detail later in this chapter. These flow factors will be assessed as separate effects but also in combination to fully understand their contributions to a decrease in thruster performance. A proper understanding of these loss mechanisms is required for completing the research objectives outlined in Chapter I.

2.3 Low Reynolds Number Flow

The concept of low Reynolds number flow has been mentioned and should be defined for this research. Reynolds number is the ratio of momentum or inertia forces to viscous forces in a flow [9]. Thrusters operating at low Reynolds numbers will experience a greater contribution of viscous forces than momentum forces. The numerator in Equation 6 represents these momentum forces in terms of mass flow or density, velocity, and area. The area can also be represented as a function of the diameter and is useful for flow through a converging-diverging nozzle. The denominator denotes

the viscous forces in terms of the dynamic viscosity of the working fluid. Equation 6 presents the Reynolds number at the throat of a nozzle:

$$Re_t = \frac{4\dot{m}}{\pi \mu d_t} = \frac{4\rho v_t A_t}{\pi \mu d_t} = \frac{\rho v_t d_t}{\mu} \tag{6}$$

This research will adopt the same definitions of low Reynolds numbers as previous research done by Grisnik, Spisz, Whalen, and Tommila in which those studies defined low Reynolds numbers as values below 10,000 [3] [5] [7] [8].

The Reynolds number in the reduced form can be driven by a change in temperature [3]. Tommila derived the Reynolds number's proportionality to the temperature and throat diameter as seen in Equation 7.

$$Re_t \propto \frac{d_t}{T} \tag{7}$$

Equation 7 shows the small throat diameters seen with micro-nozzles contribute to the large viscous forces that are driven by higher temperatures [3]. These higher temperatures are desired for electro-thermal thrusters and nozzles with larger area ratios, so the flow does not liquefy inside the supersonic region of the nozzle, reducing performance.

2.4 Viscous Losses and Surface Roughness

As discussed, low Reynolds numbers indicate viscous forces largely outweigh the momentum forces in the flow. Because these viscous forces dominate the flow behavior it is only reasonable to explore their impacts on the flow and the performance of the nozzle. Spisz defined the thrust for a small nozzle as a difference between the calculated isentropic thrust and the estimated thrust-loss term [5].

$$F = F_i - F_l \tag{8}$$

The thrust-loss term, F_l, incorporated here accounts for viscous effects and loss due to heat transfer. This experiment assumes adiabatic, ruling out the need for exploration of the heat loss term. The focus will remain on the losses due to viscous effects in this section. The thrust loss due to viscous effects is given in Equation 9 by the integral of the local shear stress, τ, over the divergent surfaces of the nozzle.

$$F_V = \int_1^{\frac{A_e}{A_{th}}} \frac{\tau A_t}{tan\alpha} d\left(\frac{A}{A_{th}}\right) \tag{9}$$

From this relation, an equation for the loss in thrust coefficient, due to viscous drag on the surface of a conical nozzle can be derived [5].

$$C_{F_V} = \frac{0.664 f_0}{(Re_{th} tan\alpha)^{1/2}} \int_1^{\frac{A_2}{A_{th}}} f_1 f_2 d\left(\frac{A}{A_{th}}\right) \tag{10}$$

$$f_0 = \gamma \left(\frac{\left(\frac{\mu_w}{\mu_{th}}\left(\frac{\rho_{th}}{\rho_0}\right)\sqrt{\frac{T_{th}}{T_0}}\right)}{\frac{2T_w}{T_0}} \right)^{\frac{1}{2}} \tag{11}$$

$$f_1 = \left(\sqrt{\frac{A}{A_{th}}} - 1 \right)^{-\frac{1}{2}} \tag{12}$$

$$f_2 = M^{1.5} \left(\frac{T}{T_0}\right)^{\frac{5\gamma-3}{4(\gamma-1)}} \tag{13}$$

These loss calculations may hold for traditionally machined rocket nozzles with lower average surface roughness but when expanding a working fluid through an additively manufactured nozzle where roughness profiles vary drastically from traditional machining, differences in performance begin to show and must be accounted for.

In previous research done by Tommila, quantification of viscous losses that include a surface roughness contribution was explored. Tommila developed an analytic model, based on Generalized Compressible Flow theory capable of predicting viscous losses with surface roughness to be used as a standard for comparison to experimental results [3] [10]. Average surface roughness of additively manufactured nozzles was measured with values ≥ 7 μm [3]. Experimental measurements of the average surface roughness for the small nozzles were only 14% higher than that of an EDM nozzle, meanwhile, the maximum height of the surface roughness in the additively manufactured nozzles was 35% larger than that of the EDM nozzle [3]. These large protrusions are dispersed throughout the internal channel and are not well captured in the measurement of the average surface roughness.

Adams, Grant, and Watson developed a method for estimating the absolute, or sand grain roughness [11]. Through experimental measurement of the average surface roughness, R_a, the sand grain roughness can be calculated as shown in Equation 14 [11]:

$$k = 5.683R_a \tag{14}$$

Tommila found that the predictions associated with Equation 14 did not accurately represent the losses experienced in the nozzle. Compressible flow losses are believed to have skewed the results of the experimental tests and have hidden the effectiveness of the sand grain roughness estimation. Minimization of these large,

dispersed protrusions may lead to results that more closely represent the predictions of Equation 14.

A follow-on study was conducted to characterize the flow through additively manufactured IN718 tubes [12]. Measurement of the effective average sand grain roughness was achieved by flowing water through the tubes. Pressure drop and mass flow were measured during the experiment. Hydraulic diameter, friction factor, and Reynolds number were calculated from the experimental results, yielding an effective relative roughness. It was found that the mean sand grain roughness varied in range from 16.04-22.24 μm. Without additional losses resulting from compressible flow effects, it seems Adams et. al's sand grain roughness estimation would result in a large overprediction of the losses due to surface roughness.

Given that this research will look specifically at the transitional and turbulent flow regimes of Reynolds numbers ranging from 2,500 to 10,000, we will utilize the Fanning friction factor. As described in Oosthuizen and Carscallen for adiabatic flow in a duct with friction, the Fanning friction factor for turbulent flow can be described in Equation 15 where D_H is the hydraulic diameter and ϵ is a measure of the mean height of the wall roughness [10].

$$f = \frac{0.0625}{\left[\log\left(\frac{\epsilon}{3.7D_H} + \frac{5.74}{Re^{0.9}}\right)\right]^2} \tag{15}$$

It should be known that the Fanning friction factor is a dimensionless representation of the wall shear stress and is a function of not only the Reynolds number, but also the roughness of the wall.

The effects of friction on a variable area flow can be related to the change in Mach number throughout the control volume.

$$\frac{dM}{M} = -\left[\frac{1+\frac{(\gamma-1)M^2}{2}}{1-M^2}\right]\left(\frac{dA}{A}\right) + \left[\frac{1+\frac{(\gamma-1)M^2}{2}}{1-M^2}\right]\left(\frac{\gamma M^2}{2}\right)\left(\frac{4f\,dx}{D_H}\right) \tag{16}$$

The above equation indicates that a change in Mach number throughout a duct, or nozzle is due to both area changes and viscosity effects [10]. The Fanning friction factor can be seen in the second term on the right side of the equation indicating the contribution of friction in the viscosity portion of the equation. This will serve as a path forward for the analytic calculation of the desired nozzle performance characteristics as created by Tommila.

2.5 Nozzle Shock Formation and Drag

This research will focus on minimizing the shock formation and drag experienced inside the divergent portion of the nozzle. Although there are loss mechanisms such as viscous loss, heat transfer, and composition or viscosity change, the losses associated with compressible shock waves and drag far outweigh the others.

In Tommila's work, he found there was very little correlation between throat Reynolds number, expansion ratio, and performance losses [3]. Tommila states this lack of correlation was likely caused by shock waves, drag, and turbulence behind the large anomalous protrusions inside the supersonic section [3].

Krishnamurty suggested, that with non-uniform surface roughness in nozzles of this magnitude, loss mechanisms such as shock waves, drag, and turbulence begin to appear [13]. It is in this type of complex flow field where viscous loss theory can no

longer accurately predict or quantify the losses experienced [13]. The performance impacts of a large protrusion inside nozzle flow were analyzed using a CFD model [4]. A 100-µm-diameter hemispherical protrusion was simulated inside the supersonic section, one throat diameter downstream of the throat. After implementing the obstruction, it was immediately recognized that multiple complex flow features had appeared. They are believed to be the key contributions to the loss of stagnation pressure and thrust inside the additively manufactured nozzles [4]. Annular expansions, bow shocks, recompression shocks, and a strong wake with high streamwise vorticity formed.

Shock wave-boundary layer interaction is noticeable in the CFD nozzle analysis [4]. Large incident shock waves that impinge a boundary layer act as a severe adverse pressure gradient imposed on the boundary layer [9]. This pressure gradient is capable of locally separating the boundary layer causing induced separation shockwaves and reattachment shock waves. Between these waves is an expansion region that turns the flow back to reattach to the surface. The boundary layer, at the reattachment point, is relatively thin with high pressure [9]. Further downstream the induced separation wave and the reattachment shock wave will merge forming the reflected shock wave noticed in the CFD study [4].

To note, multiple large protrusions were recognized when the additive nozzles were examined under a laser scanning microscope (LSM), the CFD model simulated only one such protrusion [3]. The single 100-µm surface defect led to a loss of approximately 43% in stagnation pressure across the nozzle and an overall 48% loss of thrust [4]. It is possible that more surface protrusions could lead to even more loss caused by further shock interaction.

When flow viscosity is considered, large surface protrusions can introduce drag terms inside the nozzle flow. The effects of viscosity produce two types of drag; skin friction drag, and form drag due to flow separation along the nozzle walls [9]. Skin friction drag is the component in the drag direction of the integral of the shear stress over the body [9]. Krishnamurty states that the wall roughness increases the wall shear stress and with increased roughness height there is a decrease in axial thrust. An increase in surface roughness also imparts a larger viscous boundary layer resulting in a reduction of the flow area available for the core nozzle flow [13]. Boundary layer theory does not include the drag due to flow separation and formation of vortices. Form drag can be defined as the component in the drag direction of the integral of the pressure distribution over the body [9]. This drag component can be difficult to characterize in low thrust additively manufactured nozzles and cannot be decoupled when considered with other compressible flow losses inside the expansion cone [13].

2.6 Post-Processing of Additively Manufactured Metals

Metal additively manufactured parts have been found to lead to higher average surface roughness with numerous scattered protrusions well above that average due to the laser melting process. More components are being manufactured using the additive method to capture complex part geometries that would have otherwise been extremely labor and time-intensive to make when compared to traditional machining through subtractive methods. Parts containing internal channels for flowing a fluid, such as a liquid or gas, experience unwanted flow effects due to the surface finish on the 3D printed part. Minimization of the sparse, large protrusions and high roughness is key for

desired component performance as seen in small rocket nozzles. Mechanical or electrical post-processing of these channels could lead to large protrusion size reduction and lower average surface roughness, minimizing unwanted flow effects, increasing performance.

2.6.1 EDM

Electrical discharge machining is a commonly used machining process within a variety of industries ranging from automotive and biomedical to aerospace. EDM is an electro-thermal process where a spark generated between a conductive workpiece and cutting tool removes material by melting and vaporizing the surface as spark temperatures approach 12,000 degrees Celsius. There are three main types of EDM. Plunge or ram EDM uses a positively charged electrode to erode the work part that is connected to the negative pole. Wire EDM utilizes an electrically charged wire to cut the work part. The third type of EDM is designed for drilling small but deep holes by using a rotating tubular electrode [14].

In wire EDM, the heat from the electrical discharge from a copper or brass wire vaporizes minute particles, which are then washed away by a continuously flushing dielectric fluid [15]. Wire EDM is a non-contact process with no cutting forces, permitting the production of small and fragile parts. The process results in burr-free edges, intricate details, and superior surface finishes compared to conventional blade cutting [15]. Rough cuts and skim cuts are used throughout the machining process. Rough cuts remove a lot of material, equivalent to the wire diameter plus a spark gap, because of the high amount of material coming off the part higher flushing pressure is required. This higher flushing pressure can cause wire deflection and leads to lower cut accuracy. Skim cuts are used to refine the surface after the rough cut has been completed.

Because the skim cuts are only removing a small amount of material lower, flushing pressure is used and allows for greater part accuracy. Skim cuts also use smaller sparks which allows for a stronger cutting wire with higher wire tensions, leading to better part tolerances [14].

As mentioned in section 2.4, EDM nozzles displayed lower average surface roughness and much lower peak surface roughness values when compared to the LPBF nozzles in Tommila's research [3]. Using multiple wire EDM skim cuts could lead to an even lower average surface roughness inside the throat and divergent sections of the nozzles. Figure 1 shows a typical setup for cutting a workpiece with the wire EDM technique.

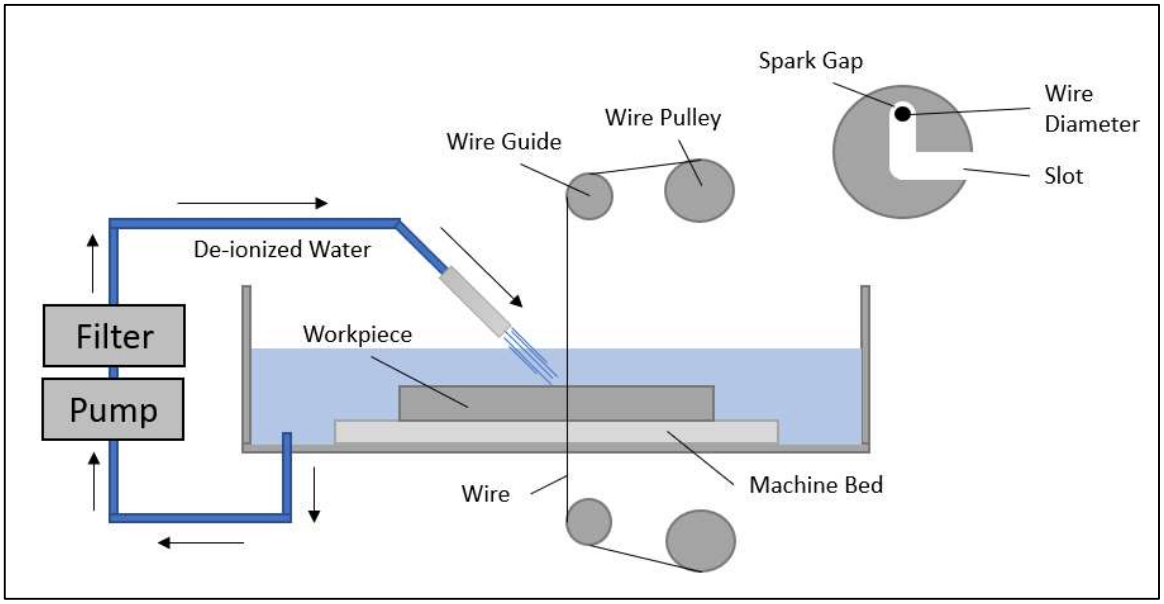

Figure 1: Wire EDM Setup

2.6.2 Abrasive Flow Machining

Abrasive flow machining (AFM) is a metal polishing process for nano-finishing, and deburring complicated geometry components, difficult to finish materials, and components with inaccessible areas such as differently shaped holes [16]. AFM is commonly used for additively manufactured parts because of the complexity of their designs. AFM uses hydraulically or mechanically controlled movement of a semi-solid, self-deformable, and pliable medium through the workpiece itself or the flow path formed between the workpiece and its fixture. Unidirectional, bidirectional, multi-flow, and orbital AFM processes are available and offer different medium flow to achieve the desired surface roughness. An AFM process consists mainly of a machine structure, workpiece, workpiece fixture, and a medium [16].

AFM material removal rates are a function of their viscosity. A higher viscosity leads to higher removal rates and a better surface finish. Several factors influence the material removal process, such as improper workpiece fixation which could lead to uneven surface finishing [17]. Other parameters such as processing cycles, piston pressure, and velocity, as well as the medium temperature and composition, including the texture of the carrier, the amount of grain, and the size of the abrasive particles also influence the result [18].

The ability to polish a part through a flow process is intriguing for small additive rocket nozzle design. The flow of medium through the nozzle could minimize surface roughness and large protrusions near the throat and beginning of the diverging exit cone

where compressible flow losses are likely higher. Uneven surface material removal and geometry change will need to be considered for this post-processing technique in the initial design. The AFM setup can be seen in Figure 2.

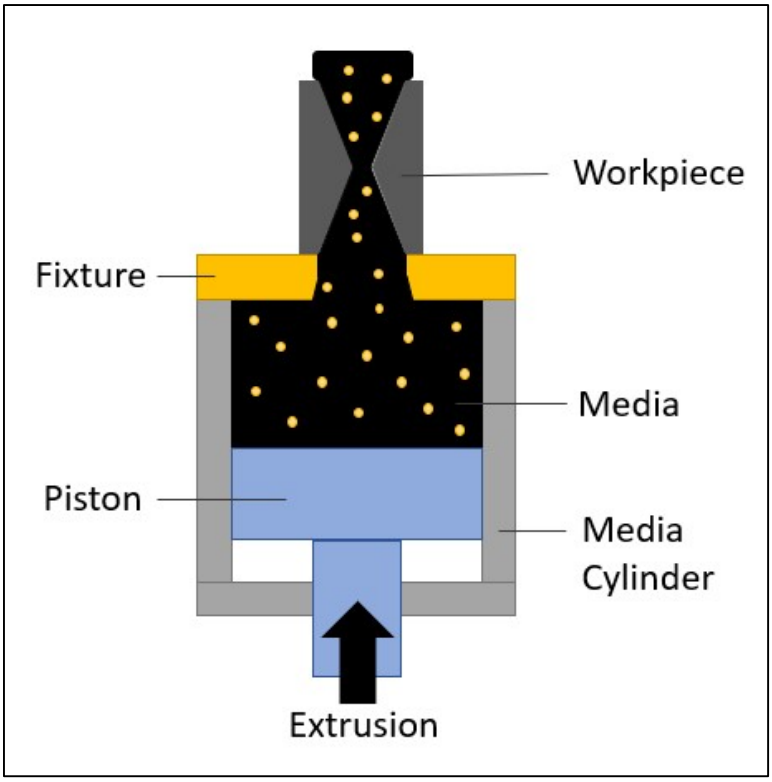

Figure 2: AFM Setup

2.6.3 Electro-polishing

Electro-polishing (ECP), also known as electrochemical or electrolytic polishing, is an electrochemical process that removes material from a metallic workpiece to polish, passivate, and deburr the metal part [19]. Electro-polishing is the reverse of an electroplating process, instead of adding material to the workpiece, the material is removed. Electro-polishing improves the surface finish of the metal by making it anodic in a suitable electrolytic solution [20]. The electro-polishing setup can be seen in Figure

3. A workpiece or anode is submerged in an electrolyte and connected to the positive terminal of a power supply. A cathode, commonly referred to as the electrode, is submerged in the electrolyte and connected to the negative terminal of the power supply. The activation of the power supply produces an electrical current that passes from the anode to the cathode, resulting in the oxidation of the metal surface and the removal of surface impurities and irregularities, which are dissolved in the electrolyte [19]. The amount of metal removed depends on several parameters including electrolyte composition, temperature, current density, time, and the material and geometry of the workpiece [19]. Current density and time are the two variables that a controlled for the electro-polishing process and can help drive consistent and reproducible surface finishes [19].

Electrolytes used for electro-polishing are often concentrated acid solutions with high viscosity [19]. A common electrolyte mixture for Nickel and Nickel Alloy parts consists of Phosphoric acid, Sulfuric acid, Hydrochloric acid, and water. Typical operating conditions for the process using this solution are 30-50 degrees Celsius and 10-18 Volts.

In a study conducted by Ali et al., electro-polishing was done on IN625 circular and rectangular tubes with diameters ranging from 7-10 mm. They polished these samples for 120 or 240 seconds and found that the internal surface roughness of the tubes was decreased by 93% during the 240-second test [21]. Ali et al. also noted a 44% reduction in sample thickness and to obtain lower average surface roughness, polishing time must increase [21]. Ali et al. recommend considering these removal rates during the design and manufacturing phases of the part that will be polished to this extent [21].

Consistent surface profiles with homogenized peaks and valleys were obtained in their research at the 120 and 240-second samples when compared to their AP states [21].

Polishing can be done on any surface of the part that has contact with the electrolyte, however, in parts with very small internal channels, it can be difficult to get the cathode within the region to effectively polish the area. The effects of the electro-polishing process on small converging-diverging rocket nozzles will be explored experimentally.

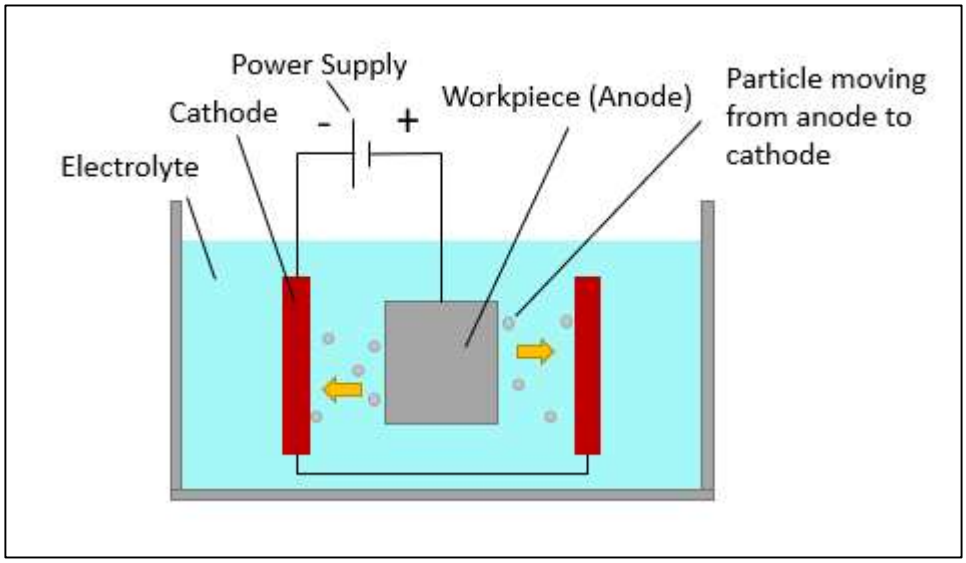

Figure 3: ECP Setup

2.6.4 High-Temperature Coatings

High-temperature coatings are used to increase performance characteristics for different components or products for their desired application. Coatings are used on parts throughout a variety of industries including oil and natural gas exploration and production, chemical manufacturing, semiconductor, automotive, and aerospace. Throughout the aerospace industry coatings have been applied to thrusters, heat

exchangers, fuel lines and delivery systems, and nozzles. Application of a coating is done to improve surface properties, increase part lifetime, and perform under extreme conditions. Coatings resist corrosion, moisture, oxidation, coking, catalysis, oil, and chemical incompatibility. High-temperature coatings are applied by processes like spraying, dipping, painting, or chemical vapor deposition (CVD) [22].

CVD is a process in which thin films are formed on a heated substrate via a chemical reaction of gas-phase precursors [23]. Applied in a vacuum chamber, the chemical reaction occurs leaving the coating applied homogenously. Because the gas fills the chamber, parts with narrow and complex passages and geometries are uniformly coated [22]. The CVD process can deposit a layer of 100 – 1,600 nanometers and withstand temperatures between 450 and 1,410 degrees Celsius [22].

Silicon-based coatings of relative thicknesses can be applied to small additively manufactured rocket nozzles. A coated layer could decrease the average surface roughness inside the nozzle, thus decreasing viscous losses. Also, the relative size of large protrusions obstructing the flow could be decreased, therefore decreasing compressible flow losses inside the diverging exit cone. Figure 4 shows the chamber where coatings are applied by the CVD process.

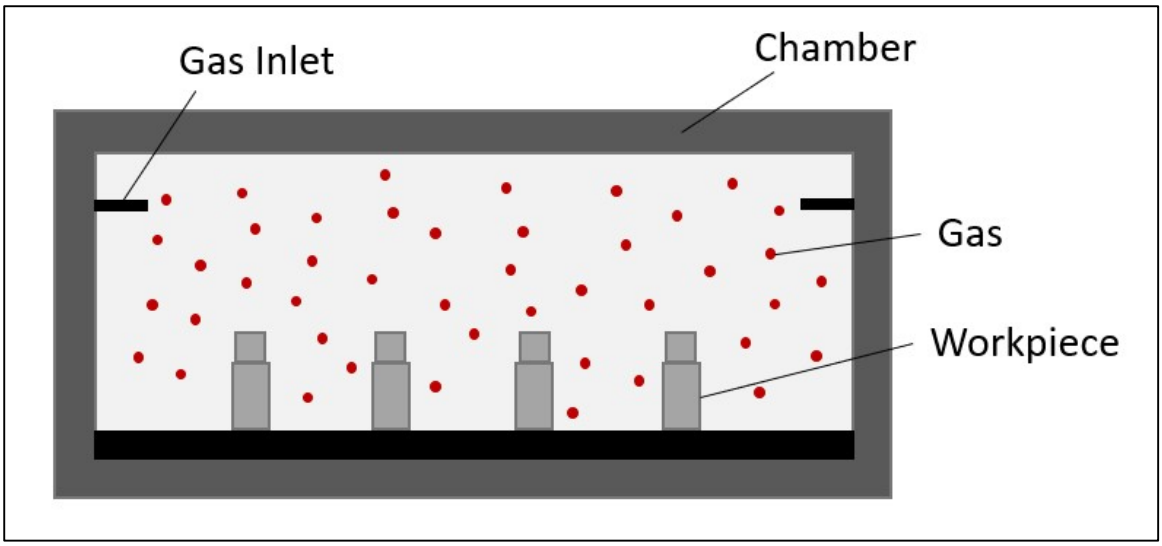

Figure 4: CVD Setup

2.6.5 Milling

Milling is the process in which a rotating tool is used to cut a workpiece. A mill commonly operates in three directions and uses a drill bit to obtain the desired cut of the workpiece. These drill bits are made of various materials and can be designed to meet machining requirements. Carbide milling cutters are commonly used in this application for IN718.

With the use of a carbide milling cutter, surface material imperfections commonly seen in additively manufactured parts can be slowly removed allowing for an improved, machine-like finish. This process could be used to improve the diverging region of the additively manufactured nozzle. A pin vise with a bit equivalent to the throat diameter could remove protrusions from the nozzle where the flow begins to turn supersonic. The combination of these could allow for a machine-like surface finish with minimal work required.

2.6.6 Post-Processing Conclusions

There are many different metal post-processing techniques throughout the metal fabrication industry. Some techniques serve subtractive manufactured parts more than additive. Because additive manufacturing is generally used for parts with more complex geometries, complex metal finishing processes are required. Removing material through different mechanical and electrical processes is possible for small additively manufactured parts as well as adding material through the use of high-performance silicon-based coatings. Although there are additional processes available, the five techniques discussed previously were determined to best suit the application for the small additively manufactured rocket nozzles used in this research.

2.7 Literature Review Conclusions

Chapter 2 summarizes the literature applicable to the minimization of compressible flow losses inside the diverging section of small additively manufactured rocket nozzles. The limitations of the ideal rocket equation and conditions required for quasi-one-dimensional adiabatic compressible flow with surface roughness were explored. Nozzle compressible flow losses caused by large protruding surface defects and the associated drag loss terms were discussed. The post-processing techniques being used for this research into minimizing the performance reduction in small additively manufactured nozzles were laid out and will be quantitatively and qualitatively examined in subsequent chapters.

III. Methodology

3.1 Overview

The purpose of this chapter is to discuss how the theory, outlined previously, will be applied through experimentation. We will utilize the thrust coefficient loss term to distinguish the performance results between post-processed and AP additively manufactured nozzles while expanding heated nitrogen gas in a vacuum chamber. Tommila's previously developed analytic model will be used for comparison to the isentropic performance condition and the experimental nozzle results. This model did not account for large sparse protrusions in the expansion section which lead to inaccuracies due to the induced compressible flow effects. Minimizing the surface defects through post-processing should lead to results more aligned with the analytic model.

3.2 Experimental Theory

For this research, we will evaluate the nozzle performance by analyzing the nozzle's thrust coefficient. The thrust coefficient was derived in Chapter 2 and is regurgitated below for reference.

$$C_F = \frac{F}{A_t p_1}$$

The three quantities on the right side of the equation are easily measurable. The thrust is measured by a load cell mounted in line with the nozzle on the thrust stand. The throat area is determined by using a stereomicroscope, measuring the semi-major and semi-minor axes of the throat. Lastly, the chamber pressure is recorded during each test run via a pressure transducer.

We are also able to effectively set the Reynolds number of the flow by heating the gas to the desired temperature and then controlling the mass flow through the throat with the use of a mass flow controller. The equation for the Reynolds number was discussed in Section 2.3 and is shown here again to highlight the relationship between mass flow and Reynolds number.

$$Re_t = \frac{4\dot{m}}{\pi\mu d_t} = \frac{4\rho v_t A_t}{\pi\mu d_t} = \frac{\rho v_t d_t}{\mu}$$

These four variables, nozzle design and geometry, mass flow through the throat, thrust output of the nozzle, and the chamber pressure, give us the ability to set the test conditions and solve for the thrust coefficient in the desired environment. The effects of area ratio, flow Reynolds number, and the post-processing technique on performance are investigated in Chapter IV.

3.3 Analytic Model Theory

One of the research objectives is to compare the thrust coefficients of post-processed additively manufactured nozzles to a quasi-one-dimensional adiabatic compressible flow analytical model with viscous losses. After experimental results were gathered, they were compared to the analytic model developed by Captain Tommila [3]. The analytic model solves for the nozzle exit conditions and thrust coefficient by solving the ODE presented in Equation 17.

$$\frac{dM^2}{dx} = \left\{\frac{M^2\left[1+\frac{(\gamma-1)M^2}{2}\right]}{1-M^2}\right\}\left(-\frac{2}{A}\frac{dA}{dx} + \gamma M^2 f\frac{P}{A}\right) \tag{17}$$

This analytic model utilizes the built-in function ode45, a Runge-Kutta method solver in MATLAB. It should be noted that in Equation 17 Mach number will decrease with an increase in flow area for supersonic flow when the friction loss term begins to dominate.

For analyzing the flow of nitrogen in the model, Equation 18 determines the dynamic viscosity. Equation 18 is a temperature-viscosity relationship that was derived from a logarithmic least squares curve fit of experimental data by Incropera and DeWitt [24].

$$\mu = (3.203 \times 10^{-7})T^{0.69898} + 4.28 \times 10^{-7} \tag{18}$$

In the model, it is assumed that the flow is fully turbulent at Reynolds numbers greater than 2000, according to Oosthuizen and Carscallen [10]. Since we will be experimenting at Reynolds numbers 2,500 or greater Equation 15 will represent the fanning friction factor for fully turbulent flow that will be ingested into the ODE.

After the model completes the necessary iterations to determine the Mach number throughout the nozzle, the exit conditions are used to calculate the thrust, stagnation temperature, and stagnation pressure [3]. With these final calculations, the thrust coefficient can be determined, thus completing the analytic process.

3.4 Experimental Materials and Equipment

This section will outline the materials and equipment used and their implementation for the experimental testing portion of this research. It will explain the reasoning behind the nozzle design and how they were tested in an inverted pendulum thrust stand. The tests were conducted in a vacuum chamber under near-vacuum conditions. A mass flow controller was used to achieve the desired throat Reynolds

number and a thermocouple for measurement of the heater block temperature capable of heating the flow of nitrogen gas to maintain a gaseous state throughout the testing process. Thrust measurements were taken by a load cell mounted to the thrust stand and stagnation pressure measurements were attained by a pressure transducer. This data was collected using LabView Software, then exported to Microsoft Excel for data reduction and analysis.

3.4.1 Test Setup

Tests were conducted in a laboratory environment. Figure 5 shows the experimental setup of the components used for the test. Propellant feed lines connect to a mass flow controller outside of the vacuum chamber. Setting the desired mass flow, the propellant then moves downstream through a port in the side of the vacuum chamber where it then enters the heater block and is increased to a temperature of 600 Kelvin. The heated propellant flows through approximately 18 inches of tubing before it reaches the entrance to the chamber. The pressure transducer relays the stagnation pressure to the data acquisition system. Then flow enters the converging-diverging nozzle and is expanded creating thrust.

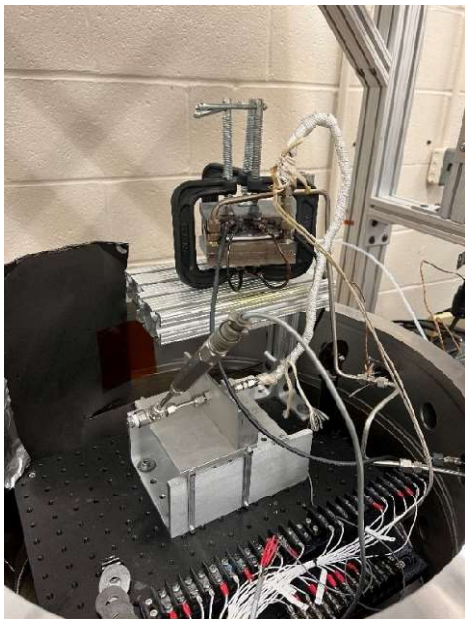

Figure 5: Test Setup

3.4.2 Nozzle Design

The nozzles designed for this experiment were done through an LPBF process on a Concept Laser M2 printer. They were designed for an efficient testing process with a 7/16-inch hex bolt design with 1/4-inch NPT threads for ease of use with Swagelok™ fittings. The ¼ inch threads were cut into the 3D printed part after manufacture as seen in Figure 6. This allowed for a clean thread finish where Teflon tape could be used for a leak-free seal. The hex part of the nozzle was redesigned from previous research.

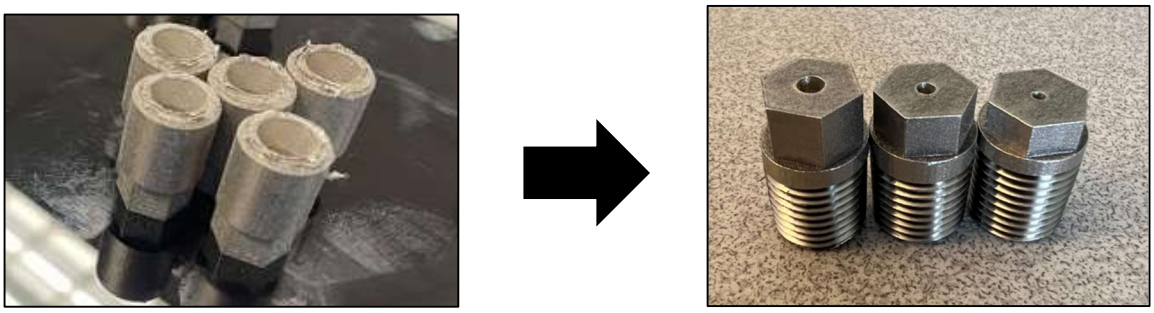

Figure 6: Nozzle Threads

The overhanging 3/4-inch hex design used in Tommila's research required the part to be printed with the exit plane of the diverging cone faced down on the print bed. This led to potentially higher roughness inside the nozzle with overhanging surfaces as the part grew. It was also found that when cutting the parts off the print bed it caused a reduction in the exit area, affecting the area ratio the nozzle was designed to. Figure 7 shows how they were printed previously and how they were printed for this research to minimize roughness and produce a nozzle most like the initial design.

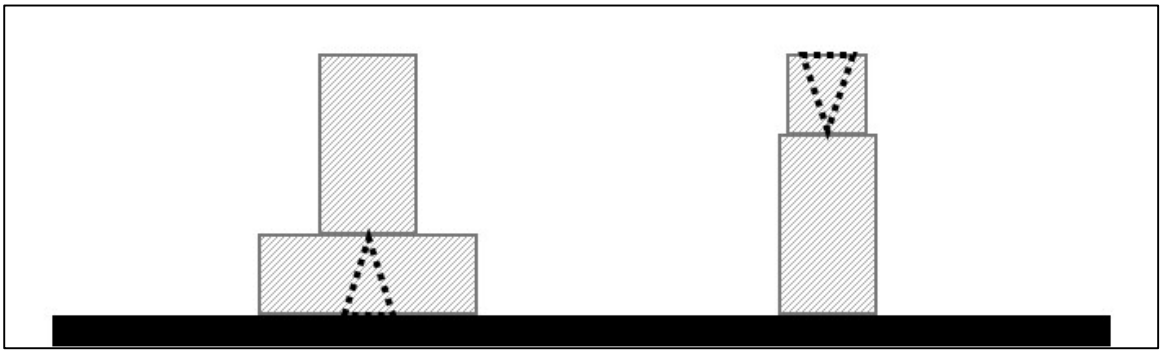

Figure 7: Thruster Print Bed Orientation

The selection of the nozzle throat diameter comes from the results of Tommila's research. A 0.02-inch throat diameter was chosen and implemented in the design of every nozzle used in this experiment. Tommila's research explored multiple throat diameters and their effects on performance. In general, the smaller throat diameter nozzles experienced greater losses than the nozzles with a larger throat diameter, presenting an opportunity to utilize post-processing techniques to reduce such losses [3].

A total of 45 nozzles were printed out of IN718, all with a 15-degree half angle diverging cone. 30 of these nozzles were printed at Vertex Manufacturing facility in Cincinnati, OH for the AP and AFM nozzles. The other 15 were printed at the Air Force Institute of Technology at Wright-Patterson Air Force Base, OH for the milled nozzles. Both facilities printed the parts on Concept Laser M2 printers. An additional two LPBF nozzles made of Haynes 282, a nickel alloy similar in composition to IN718, were used from Tommila's previous study for the electro-polishing portion of this research. Four to five parts were printed for each test case and serialized. Expansion ratios were determined by first identifying the Reynolds numbers at which we would test. In this case, 2,500, 5,000, and 10,000 were selected to test in the turbulent flow regime. These

were chosen based on the results found with Tommila's analytic model [3]. These low turbulent Reynolds numbers behaved much more closely to the isentropic scenario, therefore if we can effectively match the roughness values of the analytic model with the experiment, we could obtain thrust coefficient values near isentropic for each nozzle. With this, we were able to use data for optimal area ratios, as calculated by Spisz, for our selections of 10, 20, and 40 [5]. Table 1 lists the nozzle measurements as they were designed. Manufacturing methods and tolerances are expected to have a slight impact on the nominal designs. This was taken into consideration when controlling the mass flow rate for each test and the measurements of each nozzle are listed in Appendix A. Figure 8 shows a section view of the nozzle chamber, converging and diverging regions.

Table 1: Nominal Dimensions of Nozzle Designs

Throat Diameter (in)	Throat Area (in^2)	ε	Exit Area (in^2)	Exit Diameter (in)	Post-Processing Method
0.020	0.00031	10	0.0031	0.063	None
0.020	0.00031	20	0.0063	0.089	None
0.020	0.00031	40	0.0126	0.130	None
0.020	0.00031	10	0.0031	0.063	Abrasive Flow
0.020	0.00031	20	0.0063	0.089	Abrasive Flow
0.020	0.00031	40	0.0126	0.130	Abrasive Flow
0.020	0.00031	10	0.0031	0.063	Milled
0.020	0.00031	20	0.0063	0.089	Milled
0.020	0.00031	40	0.0126	0.130	Milled

0.015	0.00018	50	0.0090	0.107	30s Electro-polished
0.030	0.00071	50	0.0355	0.213	60s Electro-polished

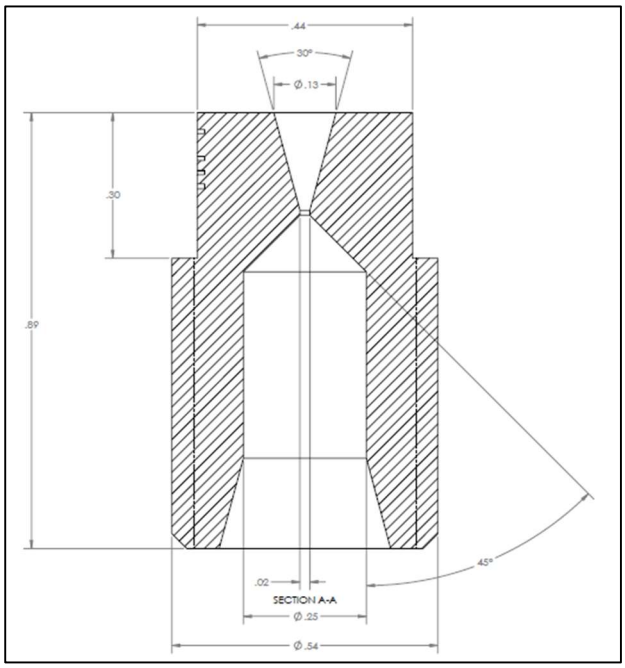

Figure 8: Nozzle Design Section View

3.4.3 Vacuum Chamber

Given the most appropriate use case for this nozzle design being small satellite operations, testing in a vacuum chamber, near-vacuum conditions presents the applicable use case with experimental results. Testing occurred in the same bell vacuum chamber as Tommila's research. This chamber complies with the volume required for the experiment while minimizing the time required to pump the chamber down to the desired test conditions. This experiment was conducted starting at pressures of approximately 26.7 Pa (0.2 Torr), pumping the chamber down with the use of a roughing pump. This pressure

helped minimize the possibility of overexpansion inside the nozzle, where flow separation losses would not be accounted for in the analysis. Air cushions were placed underneath the platform the vacuum chamber rests on. The vacuum chamber setup can be seen in Figure 9.

Figure 9: Vacuum Chamber

3.4.4 Thrust Stand

The test stand for this experiment was designed to represent an inverted pendulum system, capable of minimizing friction throughout each test run. The stand itself is bolted to a mounting plate that is installed inside the test chamber. Bolting the stand to the plate was done to minimize any vibration forces that may occur throughout the test. The stand allows for easy changing of Swagelok^{TM} fittings, making the changing of nozzles in

between tests a streamlined process. The back of the thrust stand has a load cell mounted in line with the horizontal movement of the bulkhead that seats the nozzle. During operation, the expanded gas forces the bulkhead to push against the load cell for direct measurement of the thrust force. The thrust stand can be seen in Figure 10 in its ready position with all plumbing connected.

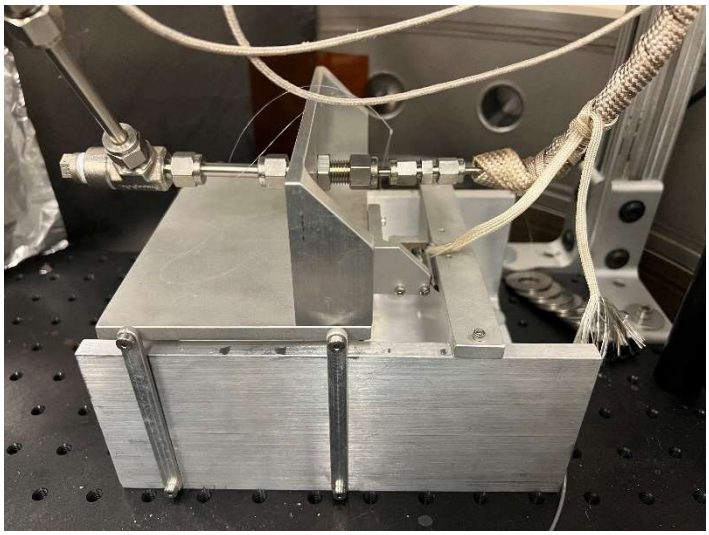

Figure 10: Inverted Pendulum Thrust Stand

3.4.5 Mass Flow Controller

A mass flow controller was utilized to set the Reynolds number for each test run. An Omega FMA5400A Mass Flow Controller was implemented to set the desired volumetric flow rate and thus mass flow rate. The volumetric flow rate is equal to the mass flow rate divided by the density of the working fluid, as seen in Equation 19

$$Q = \frac{\dot{m}}{\rho} \tag{19}$$

The mass flow rate is calculated using Equation 6, while the density of the gas is determined at standard temperature and pressure conditions. The propellant gas in this

experiment will be heated to 600 Kelvin, but the heating process takes place downstream of the mass flow controller, and therefore standard temperature and pressure are necessary for an accurate calculation. The Omega Mass Flow Controller is rated for nitrogen gas and will not require any sort of correction during the test or in the post-processing of experimental data.

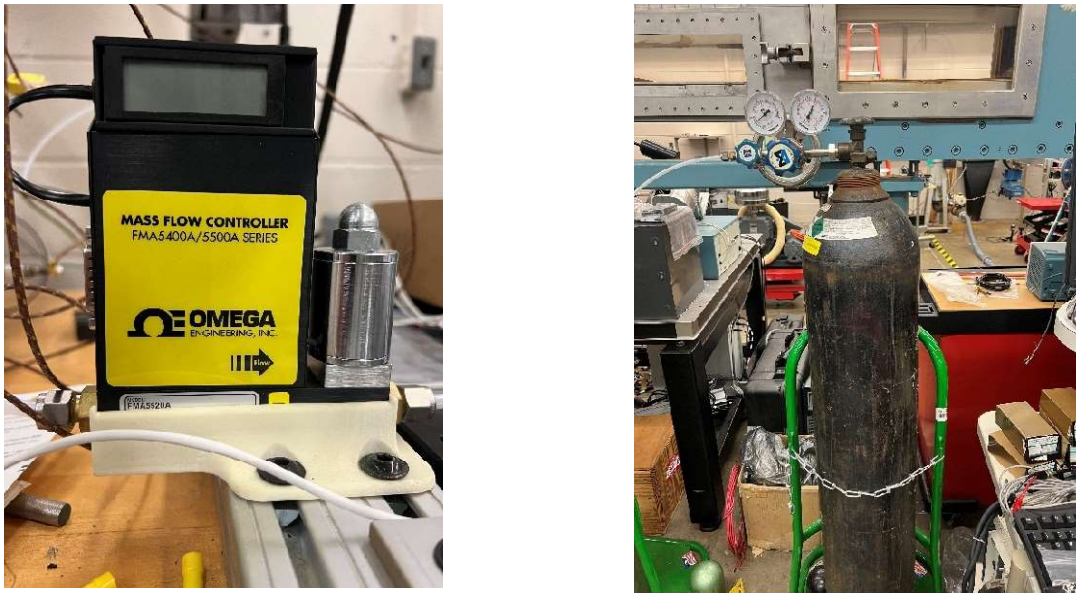

Figure 11: Mass Flow Controller (Left) & Nitrogen Gas (Right)

3.4.6 Heater Block and Thermocouple Assembly

A stainless-steel block and heater assembly were used to drive the temperature of the working fluid during the experiment. A propellant gas temperature of 600 Kelvin was desired to avoid liquefying the gas inside the nozzle during the expansion process. Two heaters are attached to the stainless-steel block and mounted inside the vacuum chamber between two ceramic blocks to aid in thermal isolation from the rest of the test platform.

The heater block temperature is measured by a K-type thermocouple attached to the rear of the block. The thermocouple relays the temperature of the heater block to the temperature controller where the temperature was monitored throughout the experiment. The proportional-integral-derivative (PID) heater controller sent the required temperature to the heaters for proper control of the working fluids temperature during the test.

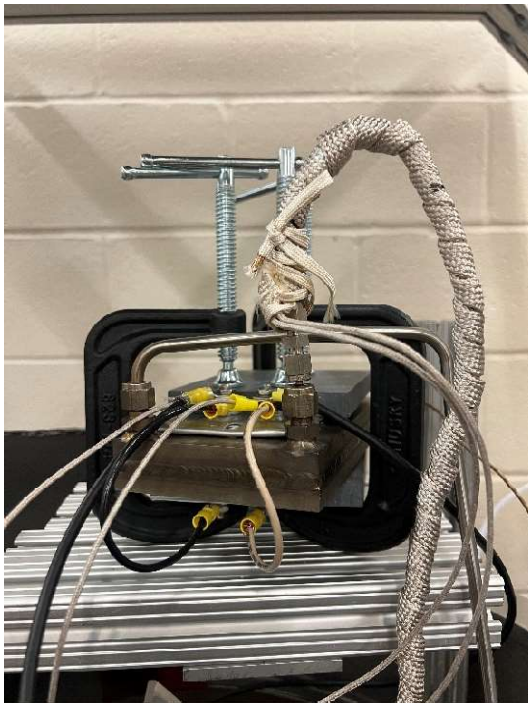

Figure 12: Heater Block Assembly

3.4.7 Load Cell and Pressure Transducer

The thrust force is measured in this experiment by a Strain Measurement Device (SMD) load cell. The load cell used was rated for a force up to 2 N. The load cell is mounted to the thrust stand where it can be measured directly when a force is applied on the inverted pendulum platform.

The load cell was installed on the thrust stand inside the vacuum chamber and then calibrated using a pulley with varying weights. More on load cell calibration is covered in the uncertainty section of this research.

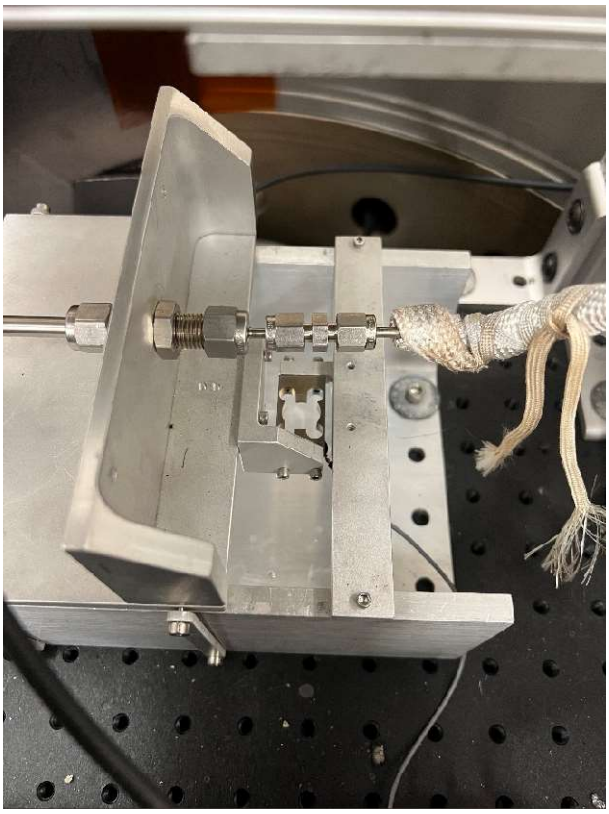

Figure 13: Mounted Load Cell

The stagnation pressure in the thruster chamber was measured by using a Honeywell A-105, 500 PSIG maximum pressure transducer along with a stainless-steel extension capable of reducing the propellant temperature, keeping it within operational limits, before reaching the transducer. More on pressure transducer calibration is explained in the uncertainty section of this research.

Figure 14: Pressure Transducer

3.4.8 Data Acquisition System

Data gathered throughout the experimental test runs were ingested into LabView using a National Instruments NI USB-6251 data acquisition system. Measurements from the load cell and pressure transducer were collected. After the LabView collection, the data was then exported to be analyzed. Data analysis techniques will be discussed in section 3.5.3.

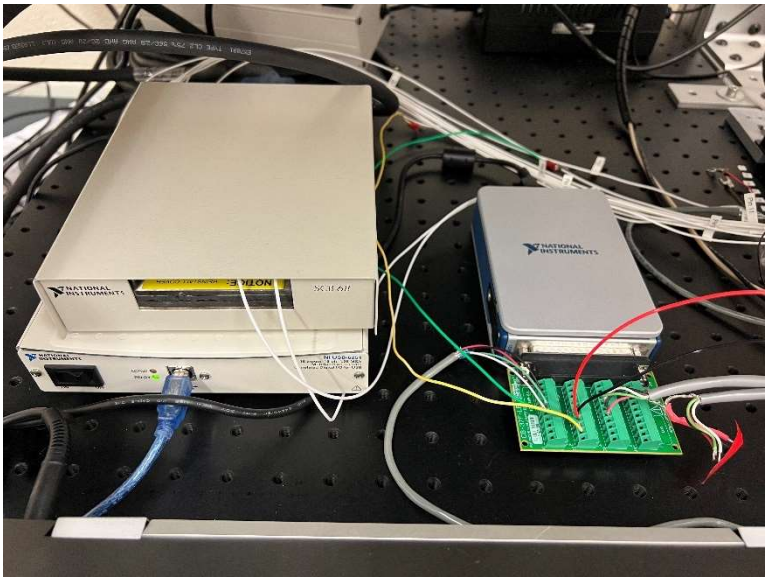

Figure 15: Data Acquisition System

3.5 Procedure and Processes

This section describes the procedures and processes taken throughout the course of this research. The overall procedure will be explained from the start of the initial design to the final measurements and data comparisons. The individual experimental tests conducted in the lab will also be explained.

3.5.1 Summary of Overall Procedure

The start of the overall procedure takes place in the initial design of the rocket nozzles themselves. Selection of the 0.02-inch throat diameter, area ratios of 10, 20, 40,

and the Reynolds numbers at which these nozzles would operate was the first step in the design and discussed in detail in Section 3.4.2. The next step was to select a working fluid and an operating temperature for the test runs. The chamber temperature was determined from the isentropic relations for an ideal rocket. The selection of 600 Kelvin allows for the selected nitrogen gas to remain gaseous inside the diverging nozzle, minimizing two-phase flow losses. Once the major nozzle parameters were identified they were modeled in a SolidWorks™ 3D CAD software and STL files were exported for the Concept Laser M2 Printers. After receiving the printed nozzles, they were examined and measured using a Zeiss Stereomicroscope. The semi-major and semi-minor axes of the throat and exit diameters were recorded and used for the calculation of the orifice hydraulic diameter. For calculation of the throat diameter, the orifice hydraulic diameter was used for a more accurate representation of what is seen due to inconsistencies in additive manufacturing of small throat diameters. Hydraulic diameter can be defined as the area of the throat divided by its perimeter.

$$D_H = \frac{4A_{ell}}{P_{ell}} = \frac{2ab}{\sqrt{\frac{a^2 + b^2}{2}}} \tag{20}$$

Once the hydraulic diameter was determined, the mass flow rate was calculated using Equation 6. With this data, the testing was then completed in the vacuum chamber using the equipment outlined in Section 3.4. Comparisons between the experimental tests and the analytic model were made and are included in Chapter IV of this research. The overall process explained above is simplified and shown in Figure 16 below.

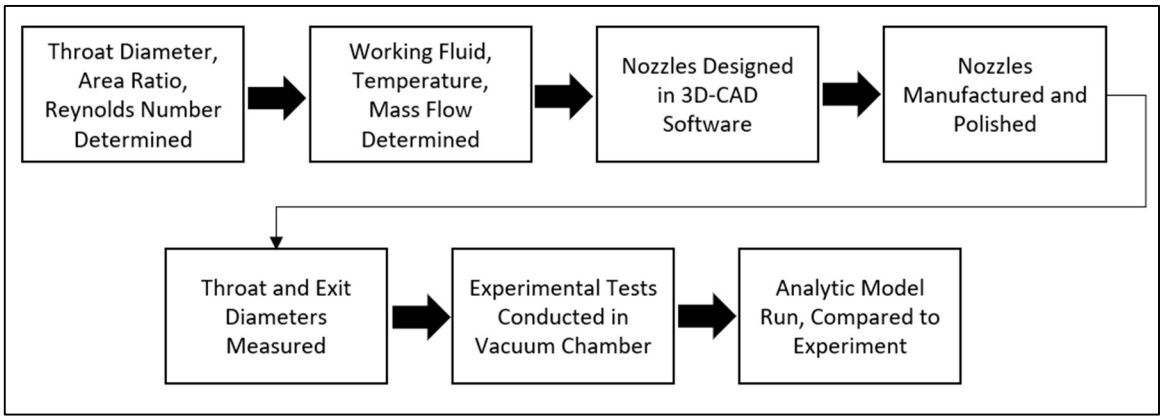

Figure 16: Summary of Process

3.5.2 Summary of Experimental Testing Procedure

The experimental testing of the nozzles is summarized in the following procedure:

1. The nozzle was mounted to the thrust stand and the pressure transducer and mass flow controller were set to the appropriate flow condition.
2. The vacuum chamber was pumped down to reach a pressure of no greater than 0.26 Torr and the heater block assembly was verified to be between 588 and 612 Kelvin.
3. The vacuum chamber pump was turned off and LabView began recording data.
4. The propellant valve was opened, allowing the flow of nitrogen gas into the system.
5. The vacuum chamber pressure gauge and the pressure transducer output in LabView were monitored.

6. Once the pressure transducer showed a steady-state condition the propellant flow was turned off.
7. The system then returned to a new steady-state condition and data recording was turned off.
8. This was repeated at three Reynolds number values per test article and then swapped out for the next nozzle being tested.

3.5.3 Data Analysis

The pressure and thrust data recorded in LabView during this experiment were exported to Microsoft Excel and analyzed. Linear regression curves were then applied to the data based on the initial calibrations. A pressure thrust term was subtracted from the thrust data to account for the rising pressure inside the vacuum chamber during operation, which was monitored and recorded outside of the LabView system. An offset in the thrust term was also subtracted away from the steady-state value. This offset term was identified by Tommila [3]. Tommila reproduced this behavior through validation during calibration of the load cell [3]. This offset term could be caused by static friction in the test stand during initial and final phases of flowing nitrogen through the system. Uncertainty in this determination of thrust is included in section 3.5.4. Figure 17 shows the steady-state and offset operations for one of the test articles.

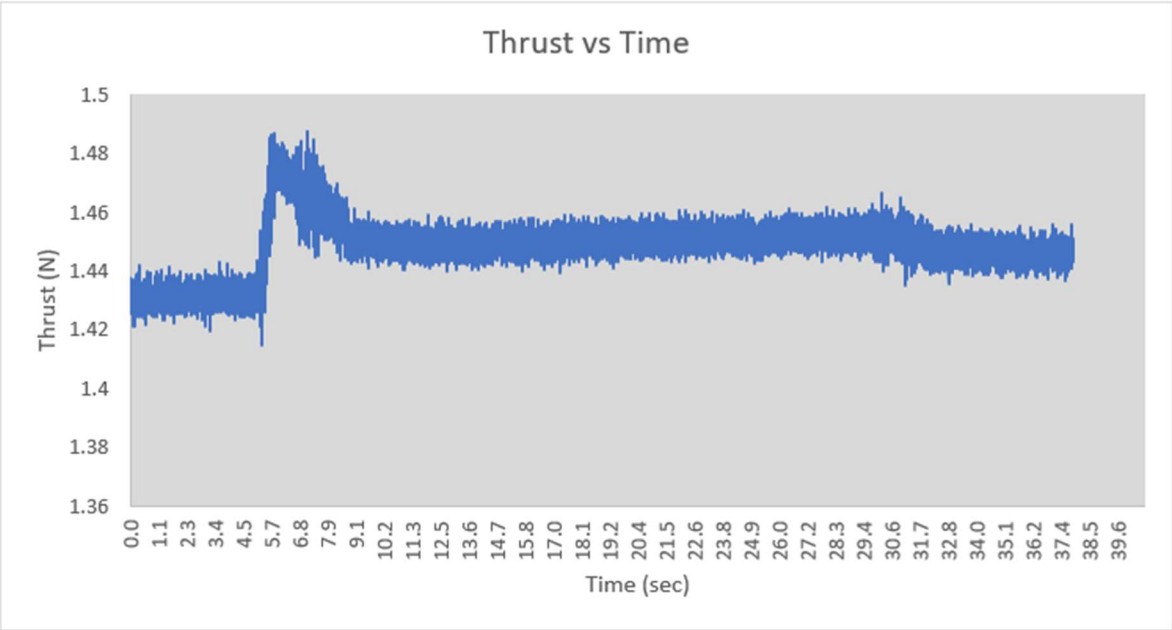

Figure 17: Thrust Data Output

The stagnation pressure and the thrust were then averaged over a range of 500 samples during steady-state thruster operation. These values along with the throat diameter measured using the stereomicroscope combined to yield the thrust coefficient, the main parameter of interest in this experiment.

3.5.4 Uncertainty Analysis

The uncertainty analysis process used for this experiment is derived from Tommila's previous research done utilizing this experimental setup [3]. The implementation of this process for this research will be explained here. This experiment incorporates both bias and precision uncertainty associated with the measurements taken.

The bias uncertainty accounts for all uncertainties within the measurement devices, including the load cell, pressure transducer, and the stereomicroscope which was

used to measure the nozzle throat diameter. The calculated precision uncertainty accounts for the variation in the measurement of the sample population.

Below are the equations listed for the bias and precision uncertainty. By taking the root sum of the squares of these values, the total uncertainty for thrust coefficient calculation in the overall experiment is obtained. This uncertainty in the thrust coefficient

$$U_B = \sqrt{U_{B,F}^2 + U_{B,P}^2 + U_{B,A}^2} \tag{21}$$

$$U_P = \sqrt{U_{P,F}^2 + U_{P,P}^2 + U_{P,O}^2} \tag{22}$$

$$U_T = \sqrt{U_P^2 + U_B^2} \tag{23}$$

is included as error bars in the plots for the experimental calculations as outlined in Chapter IV.

The load cell bias is calculated using Equation 24. The load was calibrated at small loads ranging from 0 grams to 78.9 grams with the use of a pulley system and can be seen in Figure 18. This calibration was done to ensure accurate measurement in the range of expected thrust output for the nozzles being tested.

$$U_{B,F} = \frac{F_{\max} - F_{offset}}{F_{test}} \, X \, 100 \tag{24}$$

Figure 18: Load Calibration

After carrying out the load cell calibration, an uncertainty of 9% of the applied load was determined.

The pressure transducer was also calibrated with the use of a pressurized bottle of carbon dioxide and a pressure gauge. Measurements were taken from 10 to 80 psi to evaluate the linearity and accuracy of the device. The maximum error reading during calibration was 1.1 psi. The pressure transducer uncertainty is therefore obtained using Equation 25.

$$U_{B,P} = \frac{1.1\ (PSI)}{P_{measured}\ (PSI)}\ X\ 100 \tag{25}$$

The measurement of the throat diameter was completed using the stereomicroscope which feeds the calculation of the nozzle throat area. It was determined that the

measurement process had a repeatability error in the throat area of approximately 0.0005 inches. This uncertainty is represented by Equation 26.

$$U_{B,A} = \frac{(D_M^2 + D_U^2) - D_M^2}{D_M^2} \, X \, 100 \tag{26}$$

The precision uncertainty is determined by Equation 27, which includes the standard deviation, the mean, and the number of samples in the population. $t_{\alpha/2}$ represents the t-distribution factor for a 95% confidence interval which is equal to 1.96 given a large number of samples in this analysis. The thrust, pressure, and thrust offset all contain precision uncertainty and are all included in Equation 22.

$$U_P = \frac{t_{\alpha/2} S_x}{\bar{x}\sqrt{n}} \, (95\%) \tag{27}$$

IV. Analysis and Results

4.1 Overview

This section details the results of this research and includes key findings discovered during and after the experimentation process. These results are broken down into surface finish analysis, experimental results, and the impacts of these findings. The surface finish analysis details each post-processing method and how the nozzle was affected by the respective technique. The experimental results outline what was found after flowing heated nitrogen gas through each nozzle in a vacuum environment. Some post-processing methods were not tested experimentally and are evaluated qualitatively, while other methods are quantified in this chapter.

4.2 Surface Finish Analysis

4.2.1 EDM Surface

To further understand the application of wire EDM and how it could help achieve a lower average surface roughness in small additively manufactured nozzles technicians working directly with this technology were consulted. It was determined that multiple skim cuts could help achieve the nozzle performance desired. If this were the case, nozzles could be printed without the interior channel and then be cut out using an initial rough cut, followed by the appropriate number of skim cuts to achieve an acceptable surface roughness. Four test nozzles were created using a hexagonal steel rod. The nozzles were cut using one, two, three, or four skim cuts. After the manufacture of the nozzles, they were examined under a laser scanning microscope where average surface roughness could be measured in both the throat and diverging regions. The results are

shown in Figure 19 and do not display a trend supporting the initial expectation. Neither the throat nor the diverging region presents a trend that the surface roughness decreases with an increase in wire EDM skim cuts. With this data, wire EDM nozzles were not manufactured for experimental vacuum chamber testing. A sectioned EDM test nozzle can be found in Figure 20.

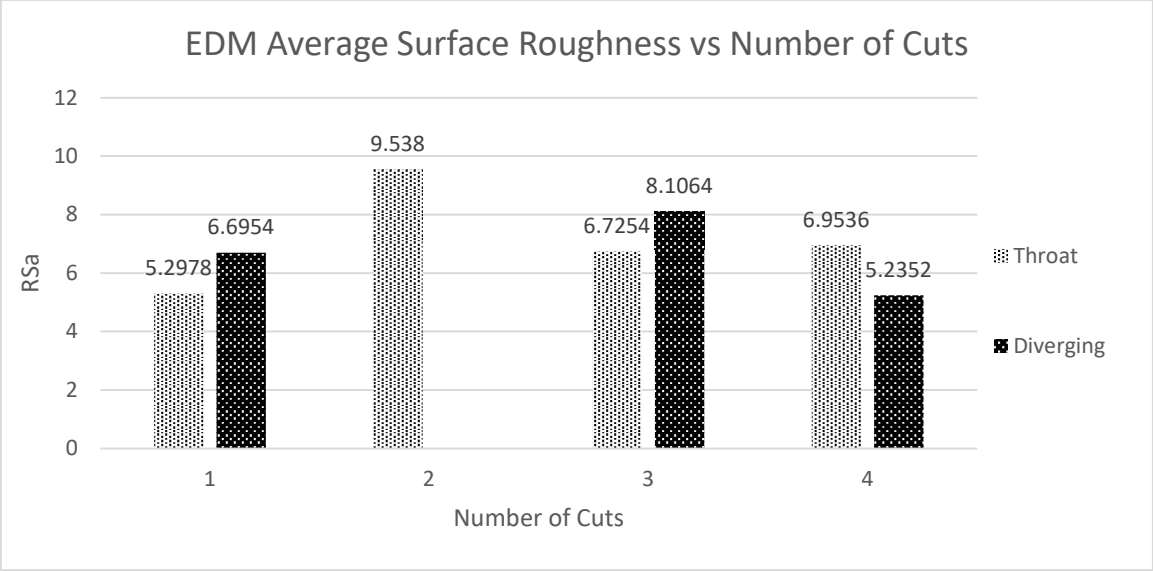

Figure 19: EDM Skim Cut Surface Roughness

Figure 20: EDM 4 Skim Cut Nozzle

4.2.2 High-Temperature Coating Surface

Various vendors were consulted to explore the application of a high-temperature coating inside the rocket nozzle. Many of these coatings would be able to endure the high temperatures of thruster continuous operation, however, many of these coatings are done using the CVD process which applies the coating material in a homogeneous layer on the order of 100-1,600 nanometers. This layer thickness applied homogeneously to the inside of the additively manufactured nozzle would result in the growth of the entire interior surface including the large anomalous protrusions which have been found to exist in these nozzle regions. These protrusions inside the nozzle diverging region are on the order of 20-150 microns. The application of a 1.6-micron layer would be insignificant

and flow protrusion and compressible flow losses would likely still occur. Figure 21 represents a 100-micron diameter hemispherical protrusion with a 1.6-micron coating applied over the throat and diverging section of a 3D CAD model of a nozzle manufactured for this research.

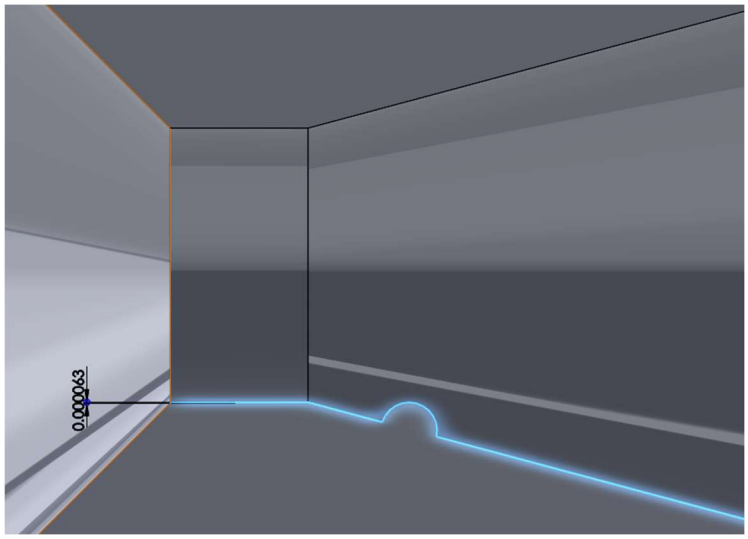

Figure 21: CVD Coating

With little expectation for significant results, nozzles were not manufactured to be coated and tested experimentally. Instead, the focus was on the manufacture and post-processing done using the ECP, AFM, and milling techniques.

4.2.3 ECP Surface

Two nozzles previously analyzed in Tommila's work were sent to Harrison Electro-polish for polishing. One of the nozzles was polished for 30 seconds and the other for 60 seconds. Working with Harrison, they determined that the cathode was unable to get near the throat or even enter the diverging region to achieve a full polishing of the part. Since the throat and diverging section were the main areas of interest for reducing the large protrusions, this method was explored only on these two nozzles and

no additional nozzles of the newer design were created. Throat diameters would need to be on the order of ¼ inch to be able to sufficiently polish the inside channel of the part. If the nozzle dimensions were changed to achieve this, it would defeat the purpose of their low thrust aspect and viscous forces would likely no longer dominate the flow. Figure 22 shows an image of the nozzle polished for 30 seconds and Figure 23 shows the diverging section of the nozzle polished for 60 seconds. This nozzle still shows various spherical protrusions varying in size that will inhibit the flow from expanding freely without shock wave formation.

Figure 22: ECP Nozzle

Figure 23: 60 Sec ECP Diverging Region

4.2.4 AFM Surface

Abrasive flow machining was explored experimentally for the decrease of large anomalous protrusions inside the nozzle. Vertex Manufacturing, based in Cincinnati, OH, printed 30 nozzles. 15 of these nozzles were tested in the vacuum chamber in their AP state and the other 15 were run through an AFM process and then tested in the chamber. These nozzles were fixed to a machine and used a conical guide to evenly distribute the pressure of the flow process inside the diverging section of the nozzle. The fixture with a nozzle mounted for the AFM process can be seen in Figure 24.

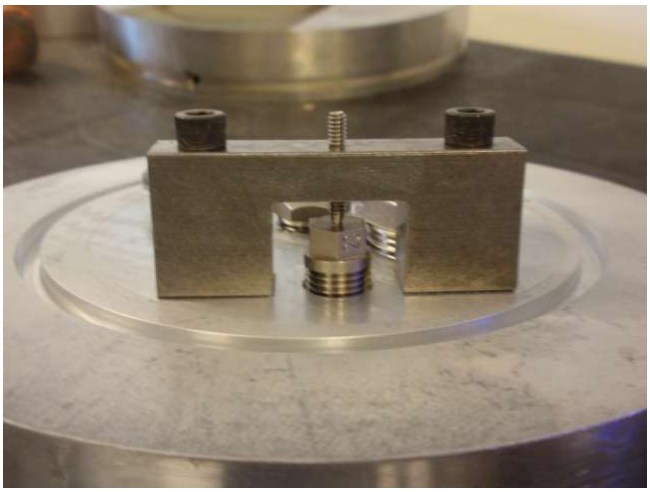

Figure 24: AFM Fixture Mounted Nozzle

The AFM nozzle throat and exit diameters were measured for further analysis. Results showed that the AFM process increased the throat diameter by 0.005” on average. Figure 25 and Figure 26 show the AFM nozzle throat and diverging sections compared to the AP nozzles as seen under the stereomicroscope. Here it is noticed that the AFM process has created a smooth-looking surface inside the nozzle and eliminated the spherical protrusions noticeable in the AP nozzles. In order to quantify the surface roughness here, the nozzles would need to be sectioned and examined under the LSM. Unfortunately, nozzles were unable to be sectioned in time for the completion of this research.

Figure 25: AFM Diverging Region (Left), AP Diverging Region (Right)

Figure 26: AFM Throat (Left), AP Throat (Right)

It was also found that the area ratio of the nozzles had changed drastically compared to the AP nozzles. The area ratio changes experienced are noted in Table 2. This area ratio adjustment can be defined by Bernoulli's Principle, knowing that the throat is undergoing a higher pressure due to the channel's reduction in area, thus increasing the throat diameter at a higher rate than the growth of the exit diameter. A sectioned nozzle can be seen in Figure 27 which shows the region that had been affected by the AFM process. In this image, it is also possible to notice the half-angle has been affected due to the growth of the throat diameter. This nozzle was sectioned at Vertex manufacturing during the initial abrasive flow tests. After receipt, it was examined under the LSM. In Figure 37, a very consistent surface profile was found at the throat although one 30-micron protrusion still remained.

Table 2: Area Ratio Change in AFM Nozzles

Area Ratio	Average Change	Standard Deviation of Change	% Change in Area Ratio
10	2.61	0.93	26.1
20	6.07	2.02	30.4
40	15.85	1.21	39.6

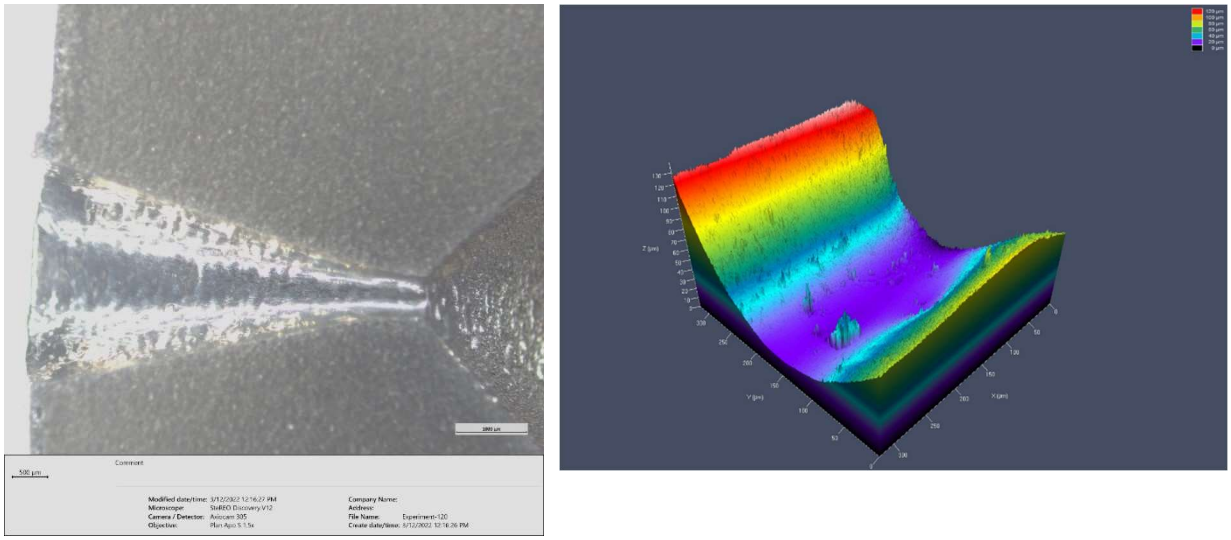

Figure 27: AFM Test Article Sectioned & Surface Roughness

4.2.5 Milling Surface

Fifteen of the 47 nozzles were printed at AFIT on a Concept Laser M2 printer. These 15 nozzles were used to explore a mechanical finishing process of the exit cone. After consulting AFIT lab technicians, a milling technique was determined to be the best option for post-processing the IN718 nozzle. A single-lip cutter tool was designed and made from standard milling cutter carbide and can be seen in Figure 28. The tool was designed with the same 15-degree half-angle as the nozzle expansion cone with a single lip capable of removing material throughout the cutting process. The single-lip cutter tool was integrated with the grinder shown in Figure 29 to properly hone the interior surface of the diverging cone.

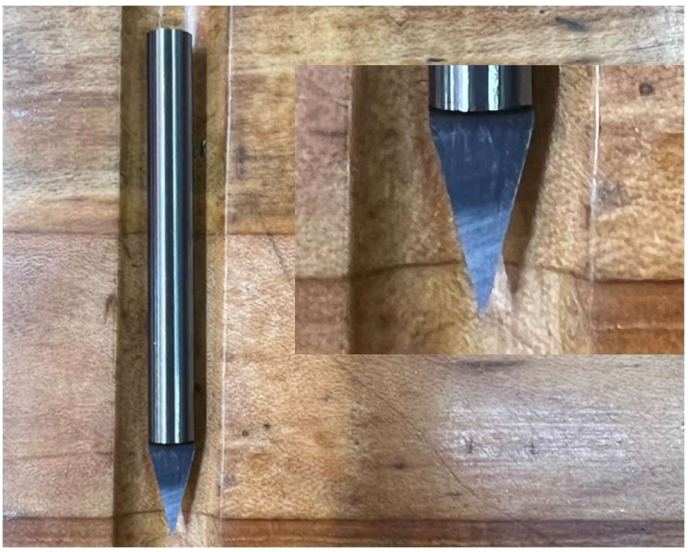

Figure 28: Single Lip Cutter

Figure 29: Deckel Grinder

To remove imperfections inside the throat of the nozzle, a pin vice with a 0.02” drill bit was used to drill out the pre-existing hole to the diameter the nozzle was initially designed to. The pin vice used can be seen in Figure 30.

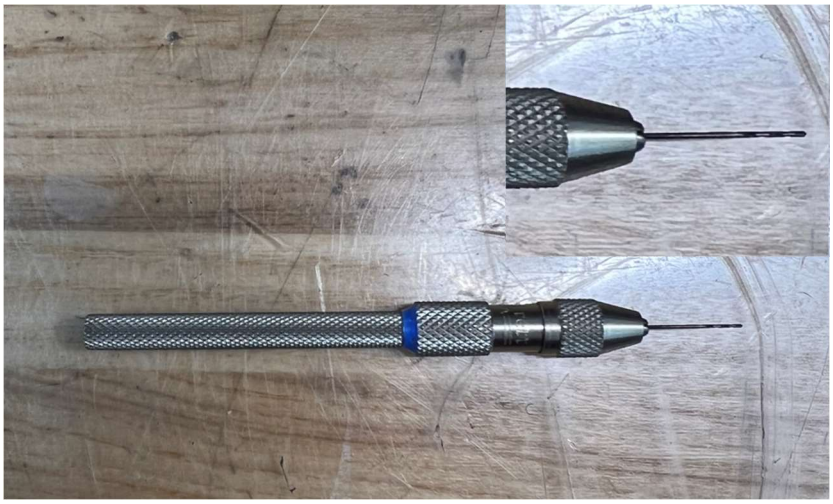

Figure 30: 0.02" Pin Vice

Analysis of the milled nozzle’s throat and exit diameters was done once their manufacture was complete. The milled nozzles exhibited very consistent throat diameters and more accurate area ratios than their initially AP state. Table 3 lays out the difference between the area ratio before and after the milling process compared to the nominally designed area ratio. With the use of the carbide single-lip cutter, it is possible to more accurately achieve the desired nominal area ratio and help maintain initial performance projections of the end product nozzle. This is shown by the significant decrease in nozzle area ratio variation.

Table 3: Area Ratio Variation in Milled Nozzles

Nominal Area Ratio	Difference From Nominal Before	Standard Deviation (Before)	Difference From Nominal After	Standard Deviation (After)	% Decrease in Variation of Area Ratio
10	1.36	1.50	0.23	0.38	82.9
20	4.24	4.04	1.59	0.71	62.4
40	7.94	4.83	1.44	0.59	81.8

Figure 31 displays the microscope focused on the diverging cone of one of the milled nozzles. In this image it is noticeable how smooth the surface appears compared to that of the AP nozzle shown in Figure 25.

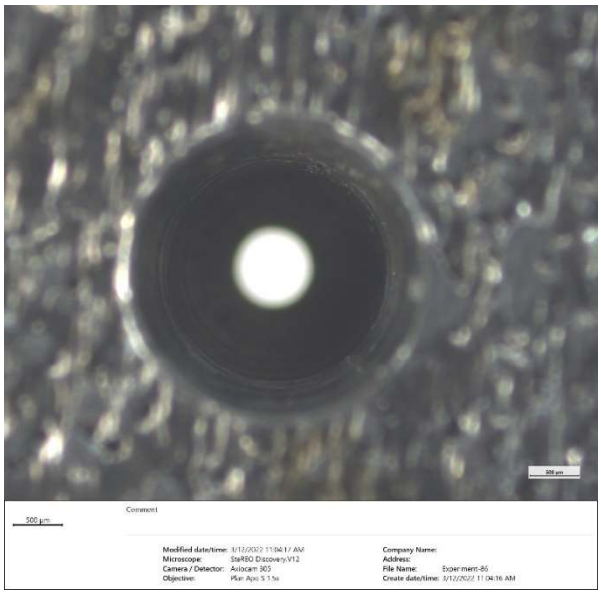

Figure 31: 20-40-5 Mill Diverging Region

It is important to note the differences between the post-processing techniques and how they may affect the initial designs of the part. The hydraulic diameter of the throat saw a large change when put through the AFM process. This change should be factored into future designs to meet the desired final product dimensions. The milled nozzles showed little change from the nominal throat diameter value of 0.02". These results are displayed in Table 4.

Table 4: Throat Diameter Change in AFM & Milled Nozzles

Method	Average Change [in]	Standard Deviation of Change	% Change from Nominal
AFM	0.0050	0.0021	25%
Milled	0.0004	0.0012	2.2%

4.3 Experimental Results

This section details the experimental vacuum chamber tests of the AP and post-processed nozzles. It will focus specifically on understanding if metal post-processing techniques can eliminate the compressible flow losses observed in low thrust rocket nozzles. Data was gathered on 4-5 test articles at each area ratio of 10, 20, and 40 and at Reynolds numbers of 2,500, 5,000, and 10,000 for nitrogen gas.

For the experimental analysis, the analytic model developed by Tommila was used as a comparative tool to determine whether the outputted data was sufficient in meeting the research objectives. Tommila's model was run using the measured average surface roughness value of 7.3-microns to determine the absolute roughness for the turbulent friction factor, according to Adams, Grant, and Watson [3] [11]. Figure 32 and Figure 33 show the analytic model output as thrust coefficient and thrust coefficient loss as a function of the nozzle area ratio. It is important to notice that the variation in thrust coefficient losses for this range of Reynolds is rather low.

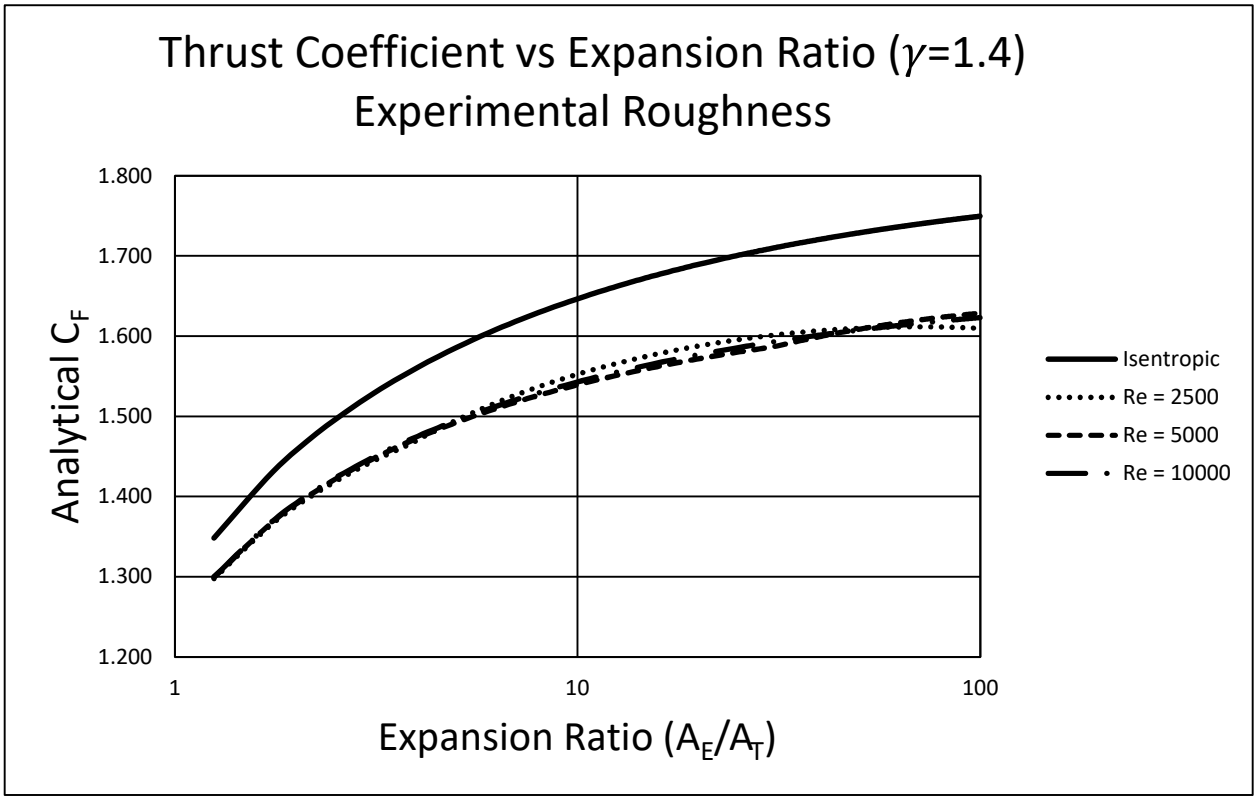

Figure 32: Thrust Coefficient vs Expansion Ratio (Analytic Model)

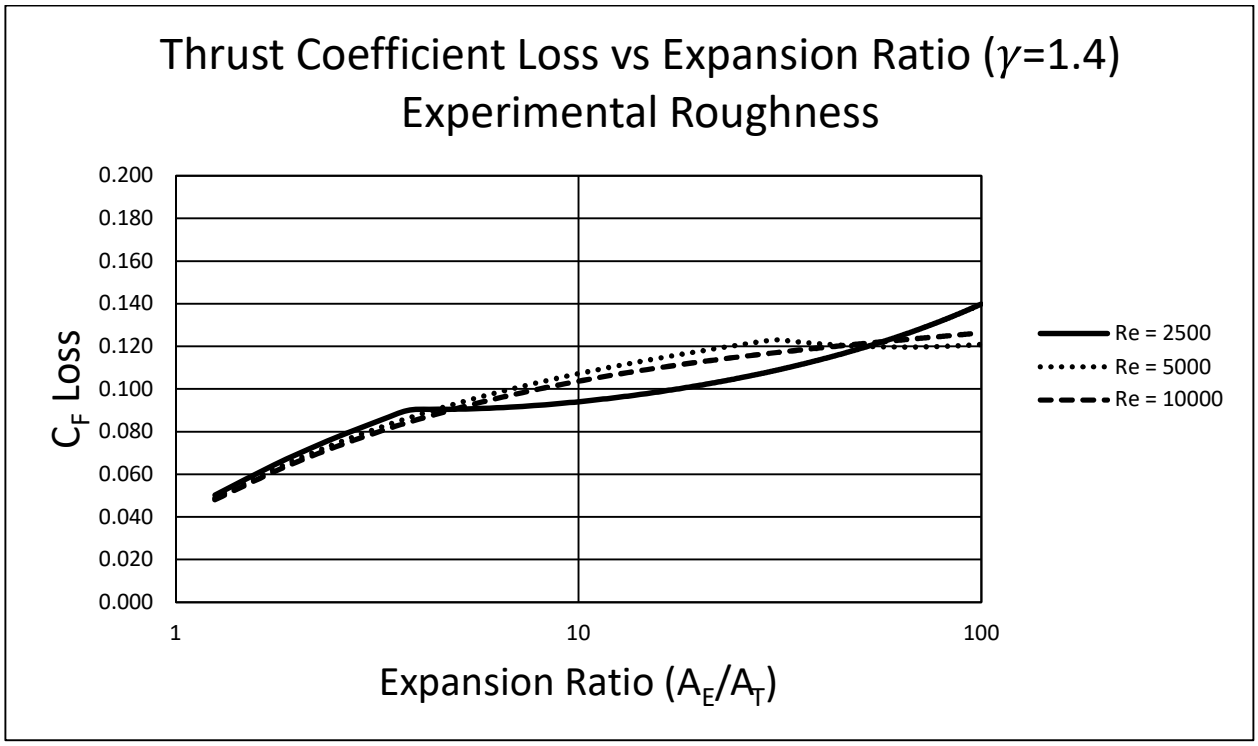

Figure 33: Thrust Coefficient Loss vs Expansion Ratio (Analytic Model)

The first observed test case is the AP nozzles at a Reynolds number of 2,500. The results in Figure 34 are similar to what was observed by Tommila, however in this case the error values are greater due to the method used in calibrating the pressure transducer. Most of the thrust coefficients for these tests ranged from 0.8 to 1.3, as expected. The milled nozzles in the same test conditions are plotted in Figure 35. The nozzles exhibited similar behavior to what Tommila had found in traditionally manufactured wire EDM nozzles where nearly all thrust coefficients are within error of the analytic model prediction at a Reynolds number of 2,500. Similar behavior was also noticed in the AFM nozzles and the plot for the 2,500 Reynolds number test can be found in Appendix A.

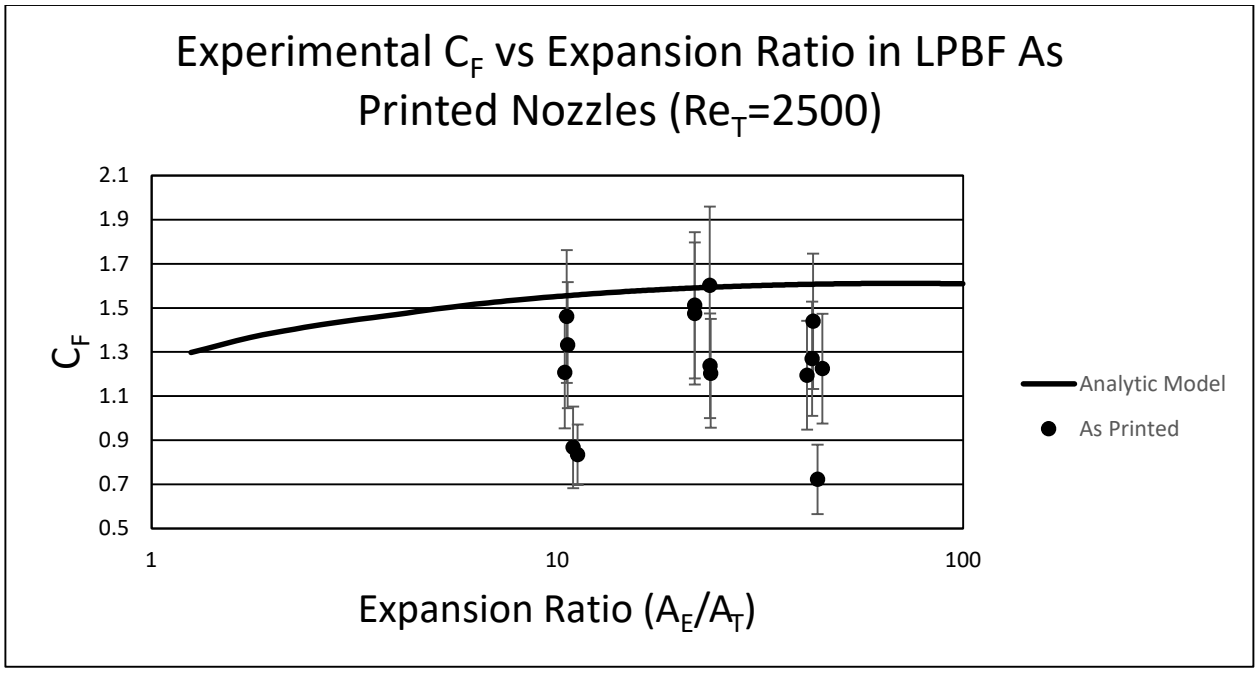

Figure 34: Thrust Coefficient vs Expansion Ratio in LPBF AP Nozzles (Re=2500)

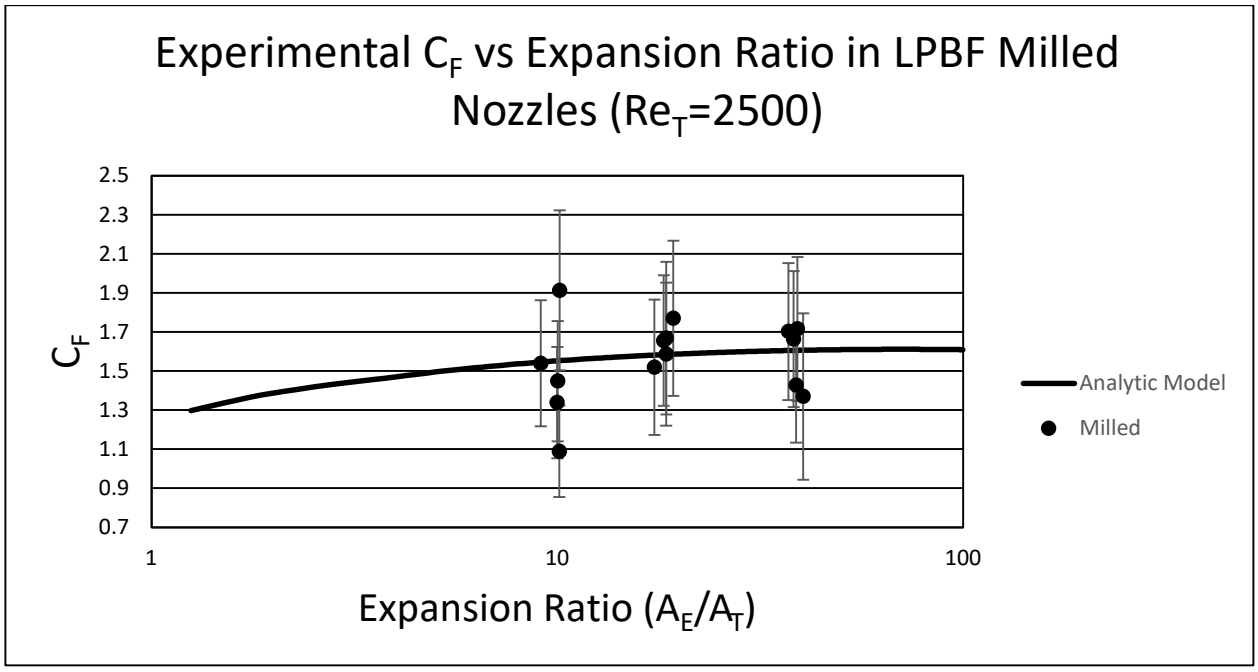

Figure 35: Thrust Coefficient vs Expansion Ratio in LPBF Milled Nozzles (Re=2500)

One key finding of this research is the decrease in thrust coefficient as Reynolds number increases. AFM nozzles at each tested Reynolds number are plotted in Figure 36. Error bars were excluded here to highlight the values of the number of varying Reynolds tests. Here there is a noticeable difference in thrust coefficient between nozzles operating at 2,500 and nozzles operating at 10,000. At the 2,500 Reynolds number, the flow is considered in the early stages of the turbulent flow regime. This is often referred to as the transition region. At the higher Reynolds number of 10,000, there are likely greater turbulent effects happening in the nozzle. It is likely that at the lower Reynolds number tests are still behaving in the laminar region, leading to a lower friction factor inside the nozzle causing higher performance [25]. Little change was noticed in performance between the 5,000 and 10,000 Reynolds numbers, but a great difference is noticed between these more turbulent values and the lower 2,500 value.

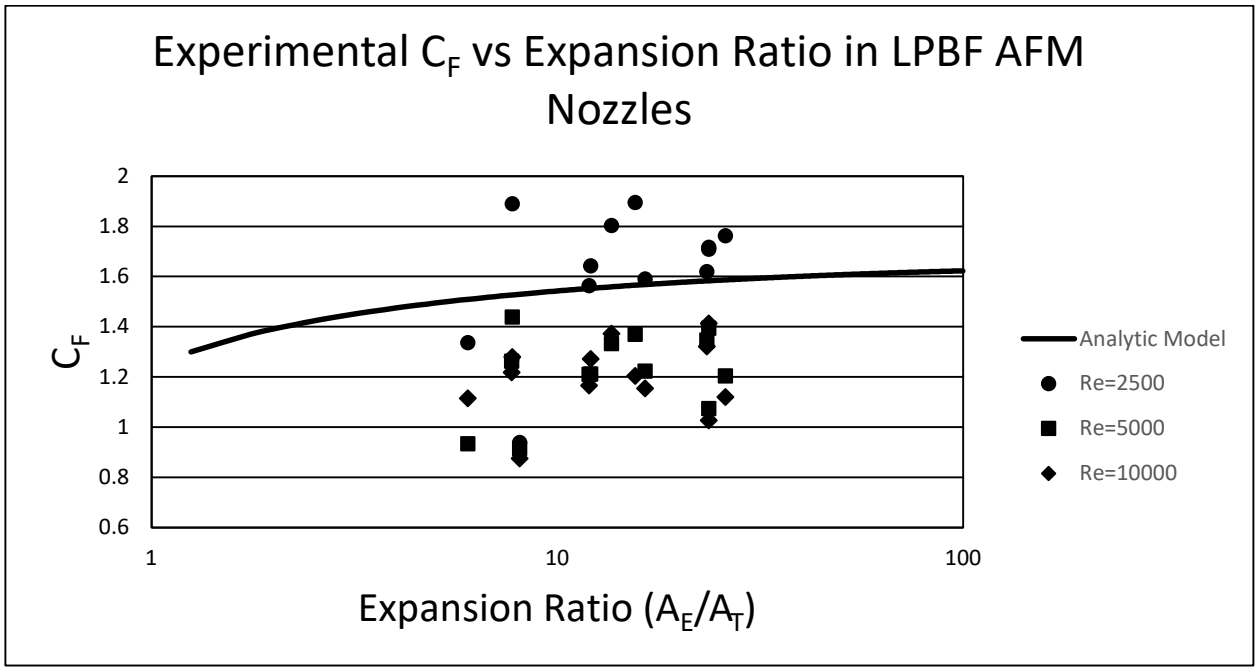

Figure 36: Thrust Coefficient vs Expansion Ratio in LPBF AFM Nozzles

One of the main research objectives was to compare the different post-processing methods to determine which provides the most performance benefit. The milling method showed consistently, across the different flow conditions, the least amount of loss in thrust coefficient. The milling data points, as seen in Figure 37, show the lowest standard deviation with values appearing above and below the predicted loss values from the analytic model. This further backs the consistency of the milling method and the high likelihood of repeatedly manufacturing a product that can provide similar results.

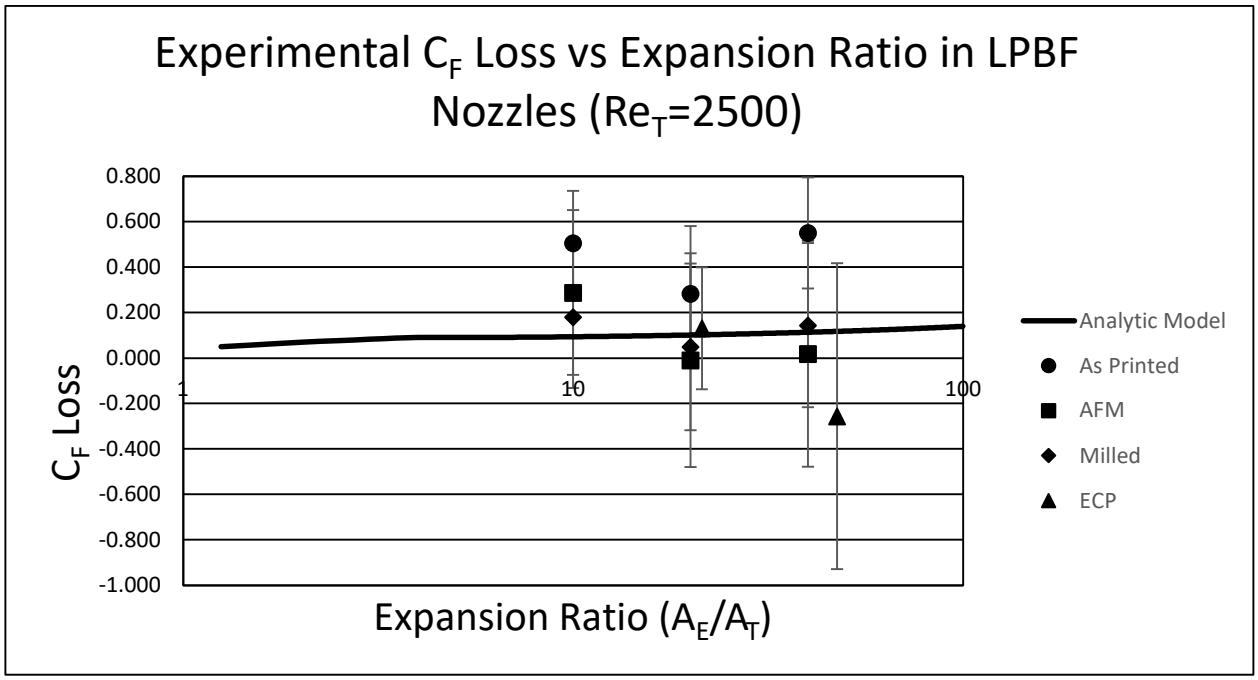

Figure 37: Thrust Coefficient vs Expansion Ratio in LPBF Nozzles (Re=2500)

Although these test values are not predicted perfectly for all tested Reynolds numbers by the analytic model, they do closely mirror the behavior of the EDM nozzles from Tommila's work. Figure 38 lays out the losses observed for those nozzles and compares them with the nozzles that had been studied in this research.

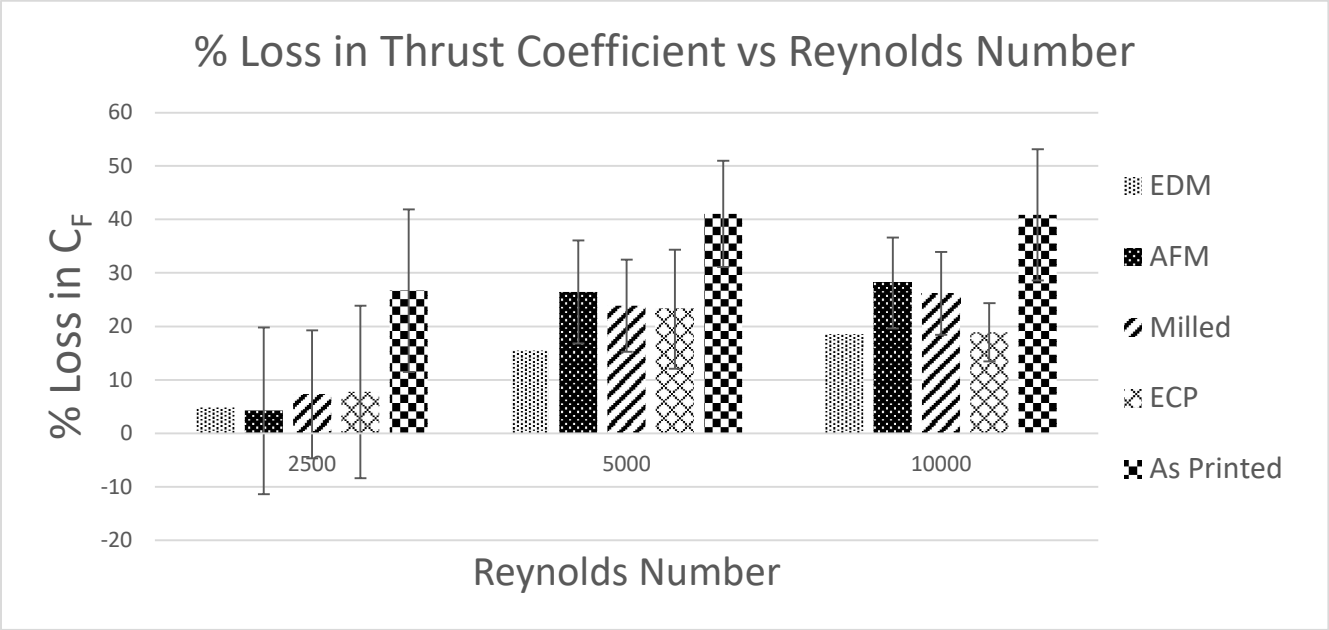

Figure 38: % Loss in Thrust Coefficient vs Reynolds Number in LPBF Nozzles

The biggest thing to note here is the drastic improvement in performance in the milled, AFM, and ECP nozzles when operating at the lower Reynolds value. It should also be stated that Tommila observed losses in the AP configuration on the order of 40% at a Reynolds number of 2,500 [3]. However, this was not the case for the AP nozzles tested at 2,500 in this research. This is likely because the nozzles are still operating in the laminar flow region, per Moody's analysis of friction factor at Reynolds numbers of this magnitude [25]. This could also be due to the orientation of the part during the physical metal printing process, as this was the only major change in the design that would have affected the performance. It is also possible the performance increase could be due to the use of a different manufacturer and could be dependent on their additive manufacturing capability. However, these are unlikely because the losses observed at the other test conditions mirror Tommila's 40% losses [3].

The two test articles for the electro-polishing process were included in the data comparison but only one nozzle test was recorded for each case Although these results suggest a much better performance than the AP nozzles, this is likely a statistical anomaly. What had been seen in the nozzle exit was still many protrusions; however, it is too difficult to tell with the naked eye if these protrusions varied in size and these nozzles will need to be further examined under the LSM. The electro-polishing process could have reduced the largest surface defects and these observed protrusions, possibly similar in size, could have been enveloped in the boundary layer. This method would need to be explored further to achieve a better statistical average across a wide range of electro-polishing times, ideally on the order of 1-5 minutes.

Table 5: Average Experimental Thrust Coefficients

Expansion Ratio	As Printed			AFM			Milled		
	2500	5000	10000	2500	5000	10000	2500	5000	10000
10	1.141	0.974	1.011	1.359	1.137	1.122	1.466	1.243	1.163
20	1.406	1.027	1.037	1.699	1.269	1.234	1.641	1.321	1.292
40	1.171	0.987	0.9471	1.702	1.254	1.220	1.576	1.281	1.275

Table 6: Standard Deviations of Averaged Thrust Coefficients

Expansion Ratio	As Printed			AFM			Milled		
	2500	5000	10000	2500	5000	10000	2500	5000	10000
10	0.279	0.177	0.247	0.394	0.257	0.178	0.302	0.126	0.120
20	0.176	0.146	0.148	0.144	0.076	0.090	0.094	0.194	0.147
40	0.268	0.210	0.238	0.060	0.145	0.178	0.164	0.134	0.132

Table 5 shows the average of all the thrust coefficients calculated in this experiment and the standard deviations of these values can be found in Table 6. Each

value represents the average of the 4-5 test articles at each area ratio. Here it is easy to notice the difference in performance at each Reynolds number when moving from left to right through the table. The highest performing Reynolds number and area ratio can also be noted. The nozzles with an area ratio of 20 consistently outperformed the others. The 20-area ratio nozzle performed best when running the experiment at the lowest mass flow rate. The milled and AFM, 20 area ratio nozzles were the highest performing nozzles of this research. This is consistent with the predictions done by Spisz for laminar-flow flat-plate theory where the optimal area ratio nozzle for flow at a Reynolds number of 2,500 was near 20. Spisz's calculations did not include losses due to compressibility which means the polished nozzles tested herein are likely only experiencing viscous losses since the behavior observed during experimental testing mirrors his predictions.

One of the most valuable outcomes of the post-processed nozzle results is the percentage increase in performance. This increase in performance is compared to the AP nozzles. Figure 39 shows the percentage increase in the thrust coefficient as compared to nozzles with no post-processing. These large increases in performance varying from 20% to 40% validate those losses were directly correlated to an increased non-uniform surface roughness of the diverging cone.

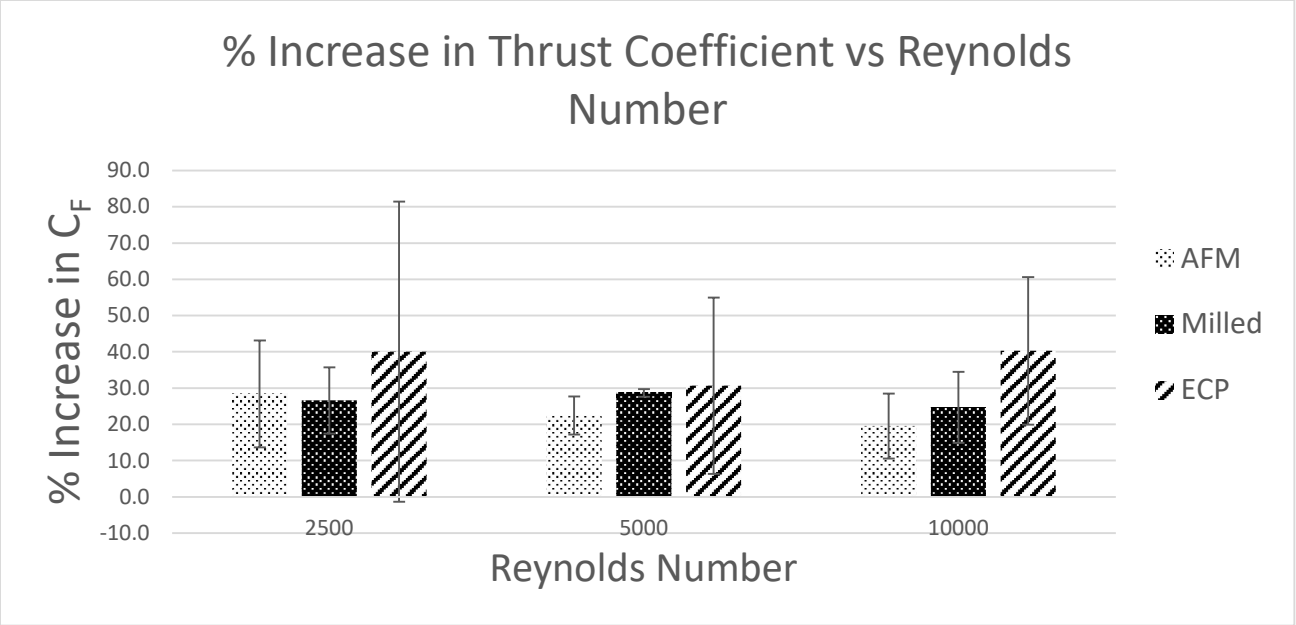

Figure 39: % Increase in Thrust Coefficient vs Reynolds Number in LPBF Nozzles

While measuring the throat and exit diameters before vacuum chamber testing a 65-micron protrusion was found in the throat of the 20-40-1 milled nozzle, likely leftover material still attached after the milling process. This nozzle serves as a prime example of losses experienced due to a large protrusion. The 20-40-1 nozzle was still tested experimentally and is seen in Figure 40. The 20-40-4 nozzle, also shown in Figure 40, was tested and compared to the 20-40-1 nozzle to identify the effects of this protrusion. The results of the measured thrust coefficients are captured in 7. This protrusion was responsible for a 5-20% difference in thrust coefficient losses experienced by the nozzles. A single test was taken at the specified flow conditions outlined in Table 7, therefore, to obtain a better understanding of the percentage loss difference more test runs likely need to occur. In the CFD study conducted by Hartsfield et al., they attributed a 48% loss in thrust due to a single 100-micron protrusion [4]. Although the 65-micron protrusion does not yield losses that high, this is still in line with what was expected and shows that even

a single protrusion just two times the size of the metal powder diameter can have a great impact on overall thruster performance.

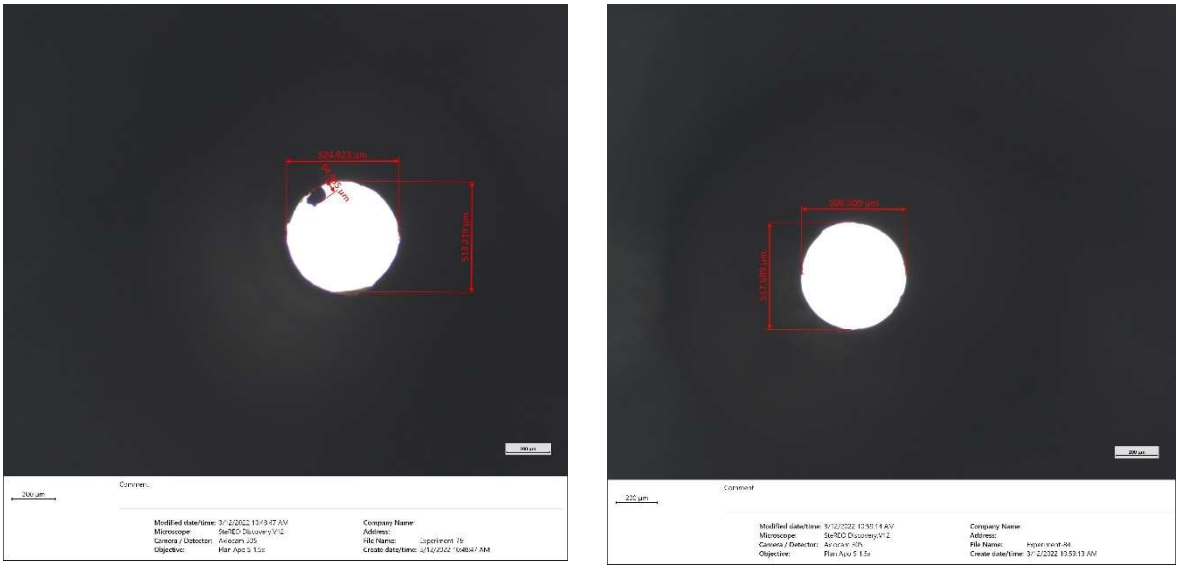

Figure 40: 20-40-1 Milled Protrusion (Left), 20-40-4 Milled (Right)

Table 7: Thrust Coefficient Loss Comparison

Re/SN	20-40-1	20-40-4	% Loss Difference
2500	1.428	1.716	16.8
5000	1.165	1.260	5.5
10000	1.057	1.404	20.1

4.4 Summary of Results

Overall, this research has shown the ability to significantly decrease performance losses in additively manufactured low thrust nozzles, especially when considering Reynolds numbers of 2,500. This improvement still does not directly match the values predicted in Tommila's analytic model for higher Reynolds numbers. This is likely due to the impossibility of removing every protrusion from the flow area in nozzles of this magnitude. Even the slightest irregularities can lead to turbulence inside the nozzle in a real-world application. Wire EDM can be considered one of the industry's most superior manufacturing processes with an immaculate surface finish. These results show the ability to achieve traditional manufacturing performance in low thrust nozzles using additive manufacturing processes combined with various surface finishing techniques.

V. Conclusions and Recommendations

This chapter provides the conclusions of this research. It reiterates and explains the completion of the research objectives, provides key findings, and lays out recommendations for future related research. 47 additively manufactured nozzles were designed, printed, and post-processed to evaluate the reduction in thrust coefficient losses due to compressible flow effects caused by large anomalous protrusions inside the supersonic region of the nozzle.

5.1 Summary of Research Objectives

The research objectives served as a pathway to successfully implement the plan determined to tackle the problem being faced by low thrust additively manufactured nozzles.

The research objectives are listed below:

1. Redesign low thrust nozzle for upright printing during the LPBF process.
2. Experimentally measure thrust and stagnation pressure of post-processed and AP additively manufactured nozzles with controlled mass flow.
3. Calculate thrust coefficients of post-processed and AP additively manufactured nozzles.
4. Compare thrust coefficients of post-processed and AP additively manufactured nozzle designs.
5. Compare the thrust coefficients between all explored post-processing techniques.
6. Compare the thrust coefficients of post-processed additively manufactured nozzles to a quasi-one-dimensional adiabatic compressible flow analytical model with viscous losses.

Research objective one was met during the initial design phase. Nozzles were redesigned using 3D CAD software so diverging exit cones could be printed in an upward configuration, minimizing surface roughness due to overhanging surfaces. Research

objective two was met during the experimental phase when laboratory testing was conducted. In the lab, the nozzles were tested inside a vacuum chamber where thrust and nozzle stagnation pressure was measured with the applicable sensors. During this phase, all manufactured nozzles were tested and data was recorded for processing. Research objectives three through six were carried out after testing and data collection occurred. Thrust coefficients were calculated from the measurements of thrust, stagnation pressure, and nozzle throat diameter. The thrust coefficients of post-processed and AP nozzles were compared, and findings were recorded in Chapter IV. All thrust coefficients and thrust coefficient losses were compared to the quasi-one-dimensional adiabatic compressible flow analytic model with viscous losses.

5.2 Summary of Results

Various post-processing techniques were explored in this research and found to positively impact thruster performance in terms of the thrust coefficient. AFM, milling, and ECP processes showed a significant impact on the resulting thrust coefficient when tested experimentally. Post-processed nozzles were found to perform better at the lowest tested Reynolds number value. The AP nozzles also showed an increase in performance specifically at 2,500. The increase in performance for the AP nozzles is attributed to the flow likely still operating in the laminar region as opposed to turbulent.

The nozzles post-processed via AFM, milling, and ECP showed similar percentage losses in thrust coefficient compared to nozzles created using an EDM process at the 2,500 Reynolds number. In the case of the AFM nozzle operating at the lower Reynolds number, it showed a reduction in overall loss when compared the EDM nozzles

at the same test conditions as seen in Tommila's work [3]. The 20-area ratio nozzle easily outperformed the 10 and 40 when operating at the 2,500 Reynolds number, in line with Spisz's predictions for optimal area ratio performance at varying Reynolds numbers [5].

5.3 Recommendations for Future Research

Design and testing of these additively manufactured nozzles have been exhausted, however, there is still research that can be explored to implement these findings into a larger design. Exploration of integrating these nozzles into a small satellite is quite possible. Already having a simple, yet effective screw-like design, these nozzles could be integrated into a satellite in need of low thrust for attitude stabilization or orbit adjustment.

Another research area that can be explored is the ability to produce a full additively manufactured electro-thermal thruster as one print or part. Rocket engine injectors are a component that can be extremely difficult to manufacture traditionally, especially for small thrusters. The ability to print an entire engine design with minimal post-processing will save cost and time. The diverging region of this full print could be post-processed using the milling method, where access from the converging end is not necessary. This full additively manufactured injector, chamber, and nozzle could yield the results of a traditionally machined three-piece rocket engine.

Although Tommila had validated the current measurement of thrust use in this research, there are other ways that should be explored in the collecting of this data given the entire nozzle performance relies on this measurement. Measuring with the use of a thrust plate should be investigated if feasible in the current test environment for these

nozzles. Also, it may be possible to calculate a thrust with measurements of velocity and pressure at various points of the flow. This may be impractical in the current test setup; however other configurations may allow for this.

5.4 Summary of Conclusions

In summary, additively manufactured low thrust nozzles can achieve performance results of traditionally machined nozzles when the use of metal post-processing of the throat and diverging region are implemented. It is important to understand where and why these results matter. These findings can lead to fully printed low thrust additively manufactured rocket engines where minimal post-processing can save significant time and cost when it comes to manufacturing and integrating low thrust propulsion technology with small satellites.

Appendix A: Nozzle Geometry & Experimental Results

Table 8: LPBF Nozzle Measurements (Stereomicroscope)

Nozzle Name	Throat a (in)	Throat b (in)	Throat Area (in^2)	Exit a (in)	Exit b (in)	Exit Area (in^2)	ε
20-10-1-AP	0.019252	0.019567	0.000296	0.062717	0.063346	0.003120	10.5
20-10-2-AP	0.025433	0.025551	0.000510	0.085276	0.085472	0.005725	11.2
20-10-3-AP	0.019567	0.019764	0.000304	0.063465	0.063543	0.003167	10.4
20-10-4-AP	0.019173	0.019173	0.000289	0.062402	0.062480	0.003062	10.6
20-10-5-AP	0.018858	0.018622	0.000276	0.061890	0.062087	0.003018	10.9
20-20-1-AP	0.019646	0.019488	0.000301	0.090945	0.091772	0.006555	21.8
20-20-2-AP	0.018465	0.018583	0.000269	0.090000	0.090512	0.006398	23.7
20-20-3-AP	0.020118	0.019213	0.000304	0.091378	0.092283	0.006623	21.8
20-20-4-AP	0.018504	0.018622	0.000271	0.090394	0.090630	0.006434	23.8
20-20-5-AP	0.018701	0.018898	0.000278	0.091732	0.091969	0.006626	23.9
20-40-1-AP	0.019409	0.019252	0.000293	0.128150	0.127638	0.012847	43.8
20-40-2-AP	0.019134	0.019370	0.000291	0.129370	0.128976	0.013105	45.0
20-40-3-AP	0.019528	0.019883	0.000305	0.129134	0.128307	0.013013	42.7
20-40-4-AP	0.019331	0.019567	0.000297	0.127047	0.126339	0.012606	42.4
20-40-5-AP	0.019764	0.019488	0.000303	0.126339	0.125748	0.012477	41.2
20-10-1-AFM	0.027244	0.028543	0.000611	0.067480	0.069331	0.003674	6.0
20-10-2-AFM	0.024016	0.023543	0.000444	0.067559	0.067638	0.003589	8.1

20-10-3-AFM	0.024370	0.024724	0.000473	0.069567	0.067047	0.003663	7.7
20-10-4-AFM	0.023347	0.024016	0.000440	0.066772	0.064803	0.003398	7.7
20-10-5-AFM	Part Not Manufactured						
20-20-1-AFM	0.027756	0.026811	0.000584	0.092480	0.096339	0.006997	12.0
20-20-2-AFM	0.027008	0.027402	0.000581	0.096063	0.093150	0.007028	12.1
20-20-3-AFM	0.022598	0.023189	0.000412	0.093032	0.092638	0.006769	16.4
20-20-4-AFM	0.023740	0.022874	0.000426	0.091969	0.091811	0.006632	15.5
20-20-5-AFM	0.025079	0.023976	0.000472	0.090236	0.090551	0.006417	13.6
20-40-1-AFM	0.025118	0.025551	0.000553	0.128110	0.130039	0.013065	23.6
20-40-2-AFM	0.024252	0.024055	0.000504	0.128425	0.128543	0.013084	26.0
20-40-3-AFM	0.026654	0.026417	0.000553	0.128622	0.127992	0.012930	23.4
20-40-4-AFM	0.026654	0.026417	0.000553	0.129528	0.128425	0.013065	23.6
20-40-5-AFM	Part Not Manufactured						
20-10-1-Mill	0.020039	0.020236	0.000318	0.063622	0.064449	0.003220	10.1
20-10-2-Mill	0.020000	0.020433	0.000321	0.064370	0.063465	0.003209	10.0
20-10-3-Mill	0.019921	0.020394	0.000319	0.060669	0.060945	0.002904	9.1
20-10-4-Mill	0.020000	0.020000	0.000314	0.063425	0.063189	0.003148	10.0
20-10-5-Mill	0.020158	0.019606	0.000310	0.063071	0.063465	0.003144	10.1
20-20-1-Mill	0.021732	0.021654	0.000370	0.090000	0.090669	0.006409	17.3
20-20-2-Mill	0.019961	0.020551	0.000322	0.087008	0.087480	0.005978	18.6
20-20-3-Mill	0.020827	0.021221	0.000347	0.089882	0.089882	0.006345	18.3
20-20-4-Mill	0.020236	0.020394	0.000324	0.089094	0.089449	0.006259	19.3

20-20-5-Mill	0.020827	0.021260	0.000348	0.090709	0.090512	0.006448	18.5
20-40-1-Mill	0.020669	0.020197	0.000328	0.127047	0.127323	0.012705	38.7
20-40-2-Mill	0.019921	0.020276	0.000317	0.127638	0.127717	0.012803	40.4
20-40-3-Mill	0.020315	0.020433	0.000326	0.125276	0.126654	0.012462	38.2
20-40-4-Mill	0.019921	0.020354	0.000318	0.125669	0.126063	0.012442	39.1
20-40-5-Mill	0.020669	0.020669	0.000336	0.125197	0.126575	0.012446	37.1
15-50-1-ECP	0.014764	0.014803	0.000172	0.068189	0.068583	0.003673	21.4
30-50-1-ECP	0.030354	0.031614	0.000754	0.080591	0.214000	0.035779	20.4

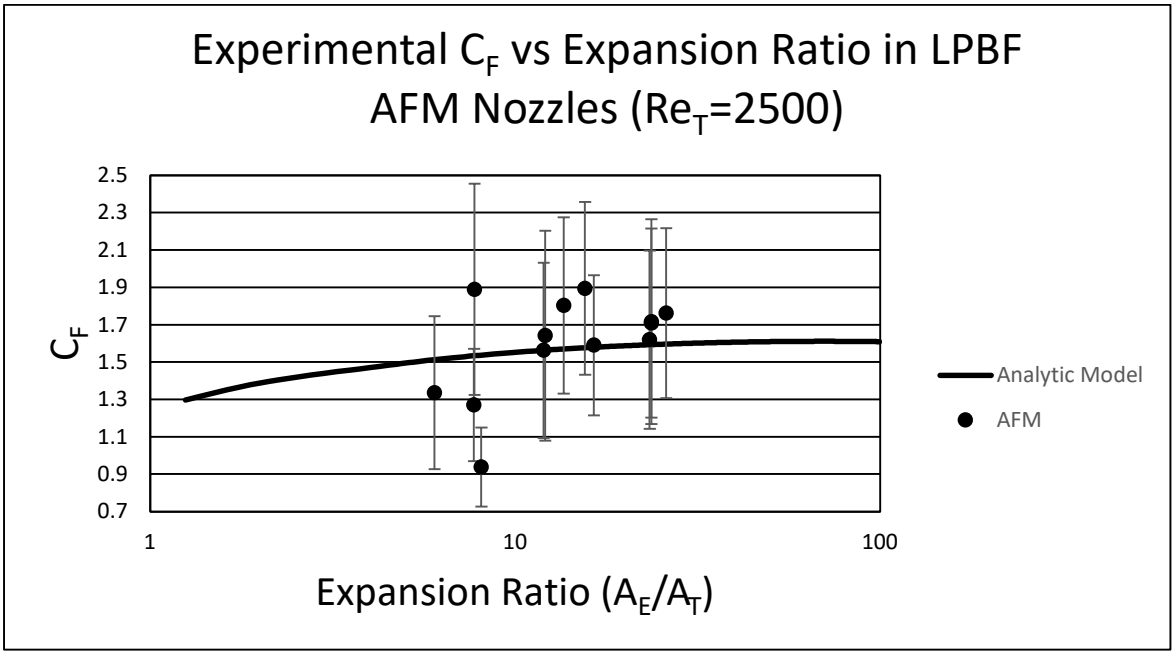

Figure 41: Thrust Coefficient vs Expansion Ratio in LPBF AFM Nozzles (Re=2500)

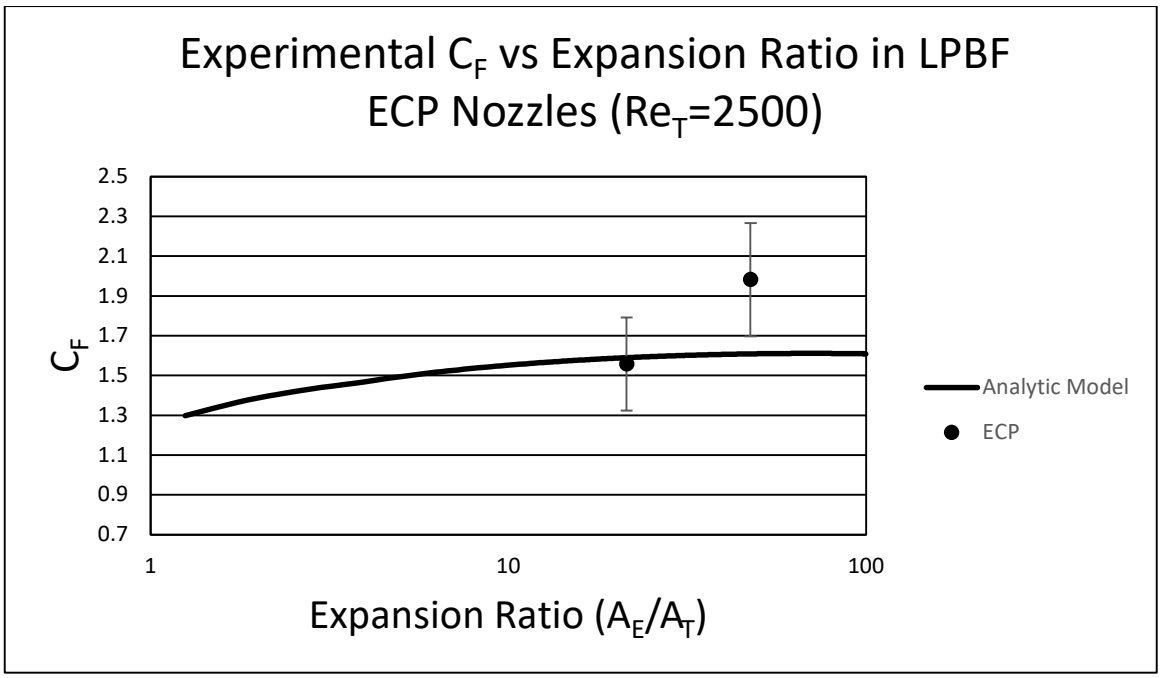

Figure 42: Thrust Coefficient vs Expansion Ratio in LPBF ECP Nozzles (Re=2500)

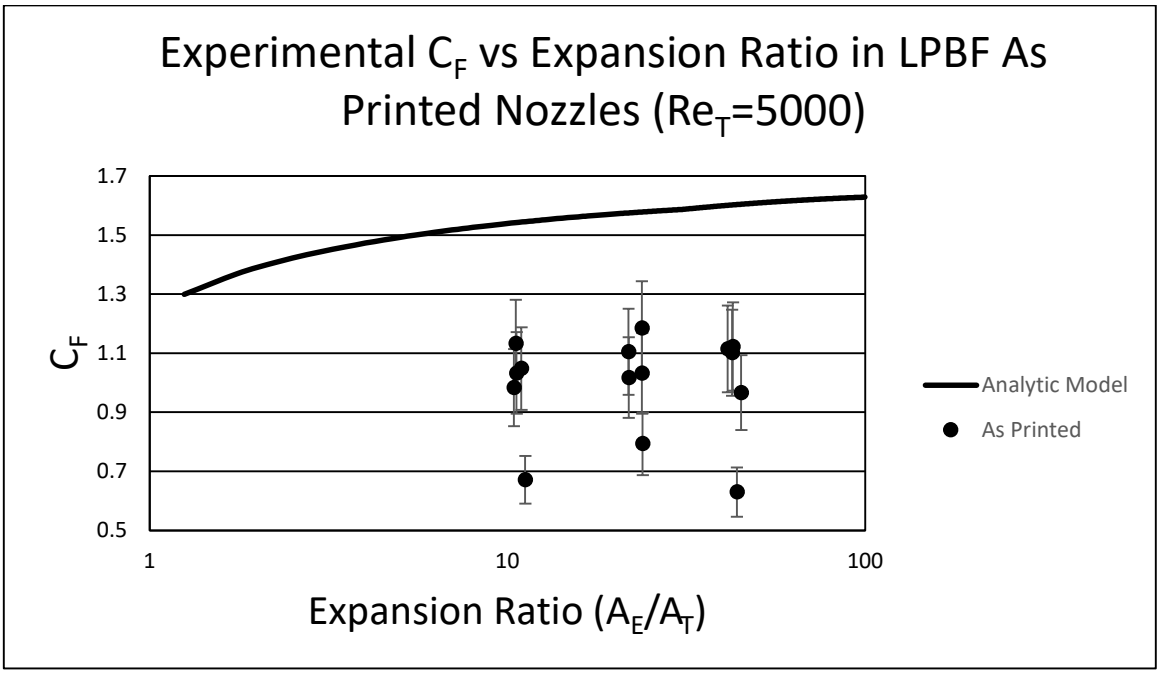

Figure 43: Thrust Coefficient vs Expansion Ratio in LPBF AP Nozzles (Re=5000)

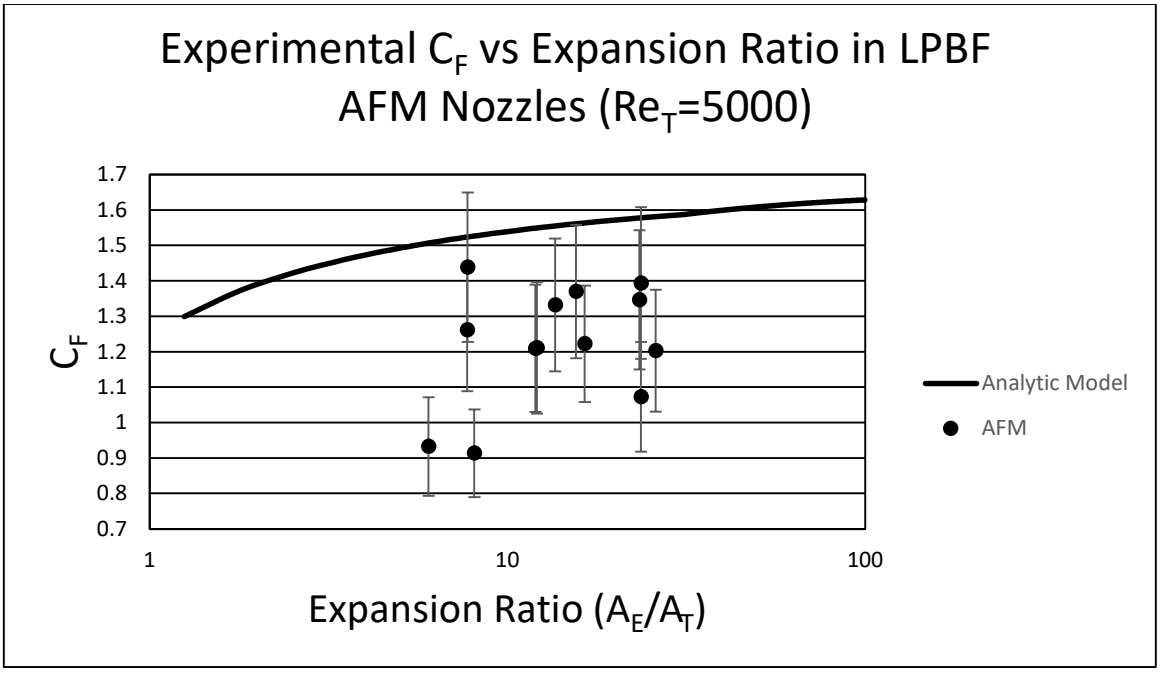

Figure 44: Thrust Coefficient vs Expansion Ratio in LPBF AFM Nozzles (Re=5000)

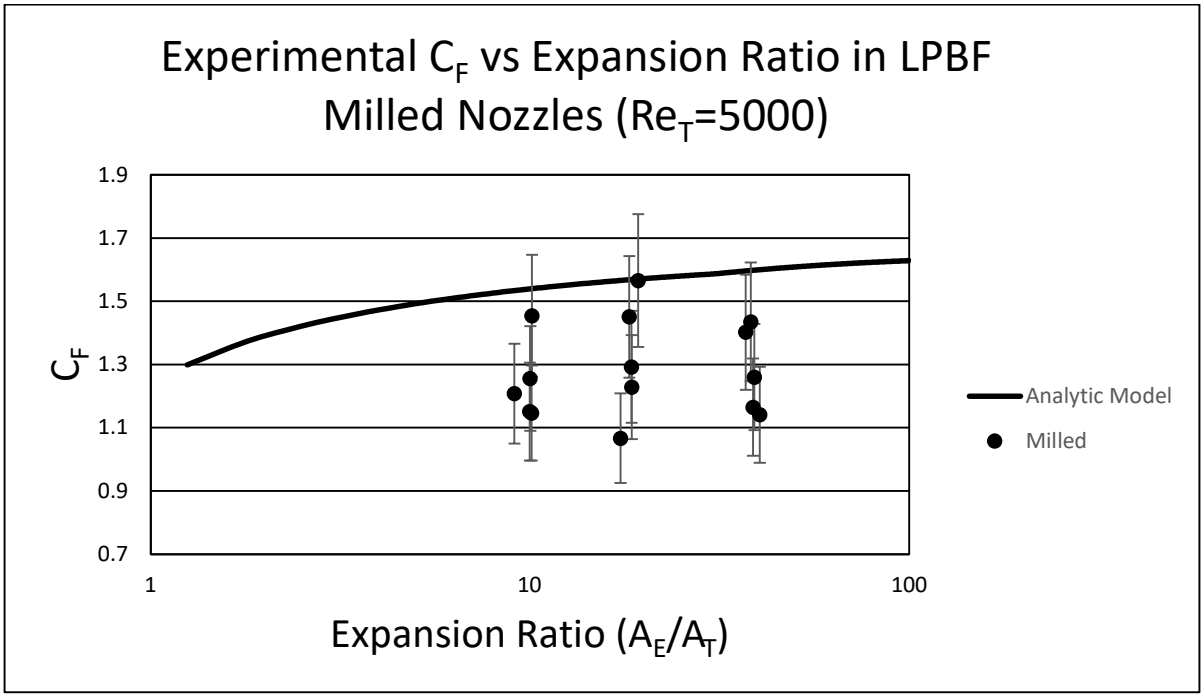

Figure 45: Thrust Coefficient vs Expansion Ratio in LPBF Milled Nozzles (Re=5000)

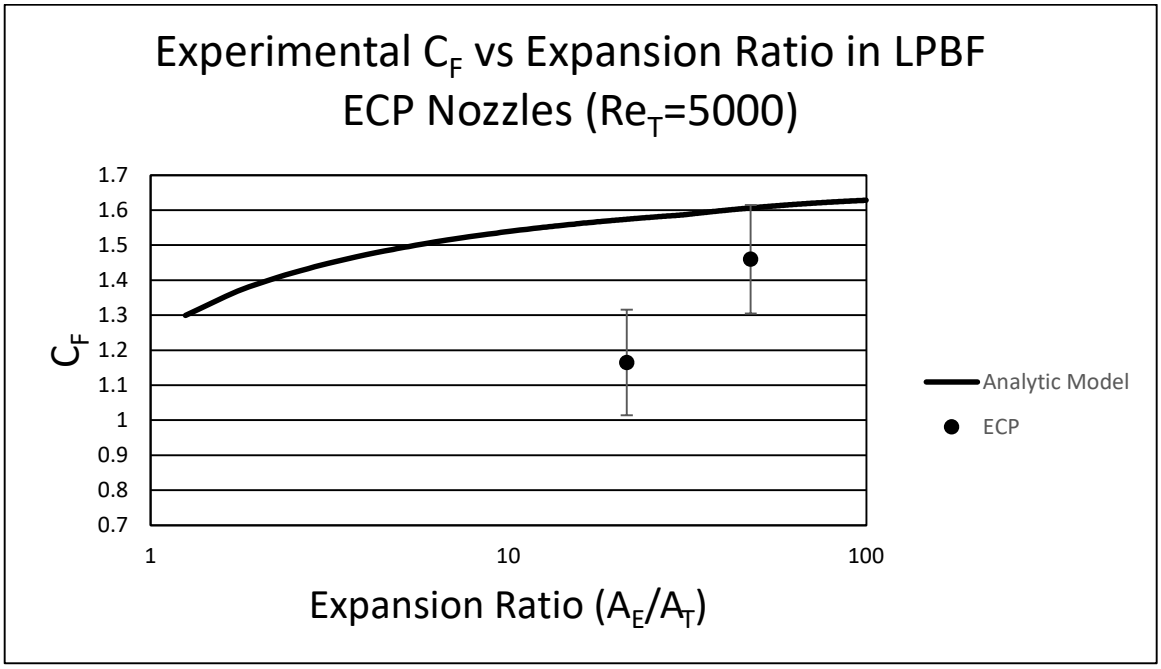

Figure 46: Thrust Coefficient vs Expansion Ratio in LPBF ECP Nozzles (Re=5000)

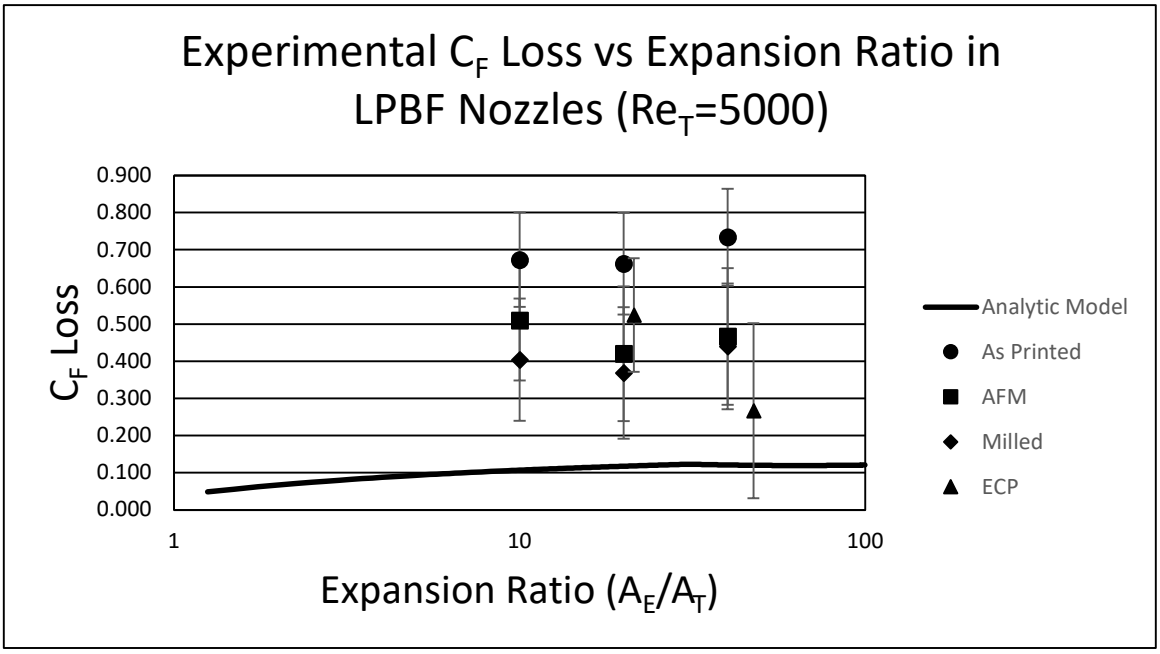

Figure 47: Thrust Coefficient Loss vs Expansion Ratio (Re=5000)

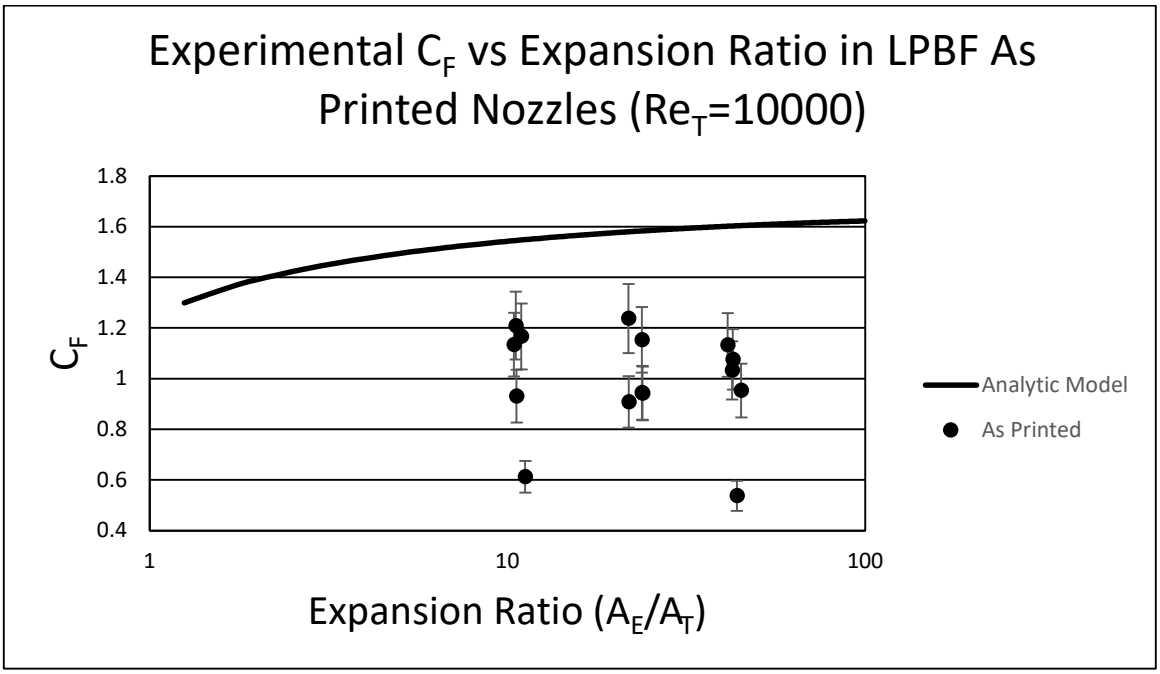

Figure 48: Thrust Coefficient vs Expansion Ratio in LPBF AP Nozzles (Re=10000)

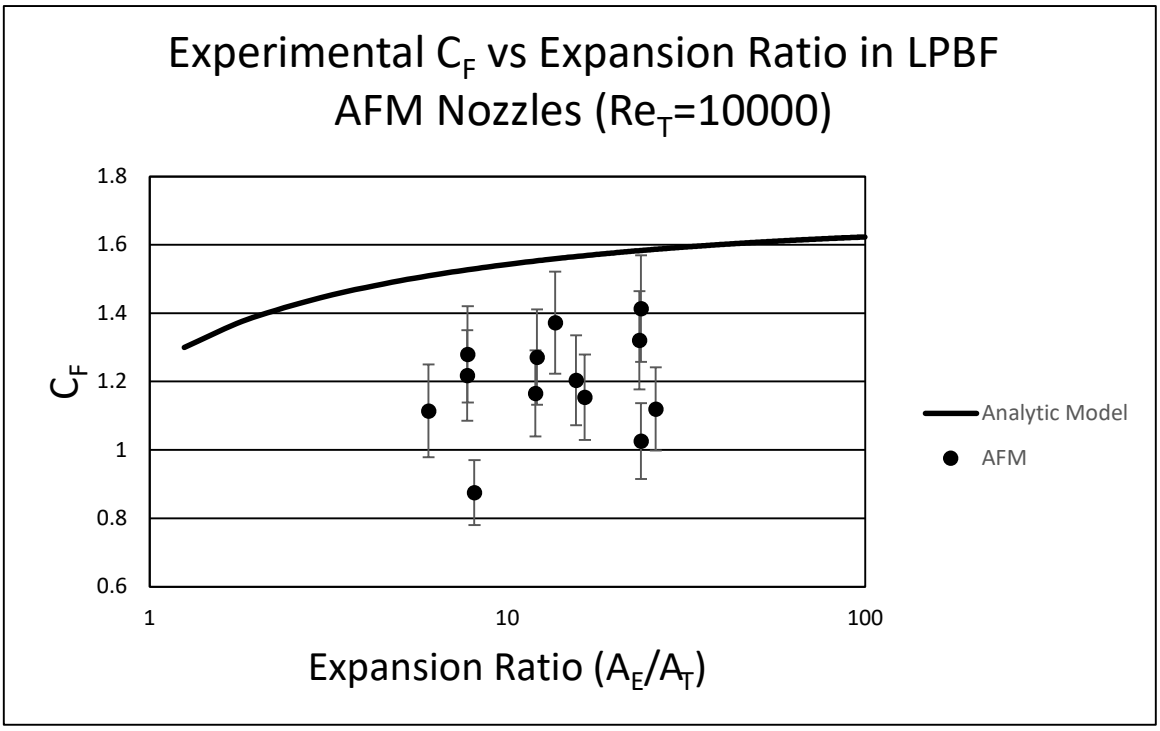

Figure 49: Thrust Coefficient vs Expansion Ratio in LPBF AFM Nozzles (Re=10000)

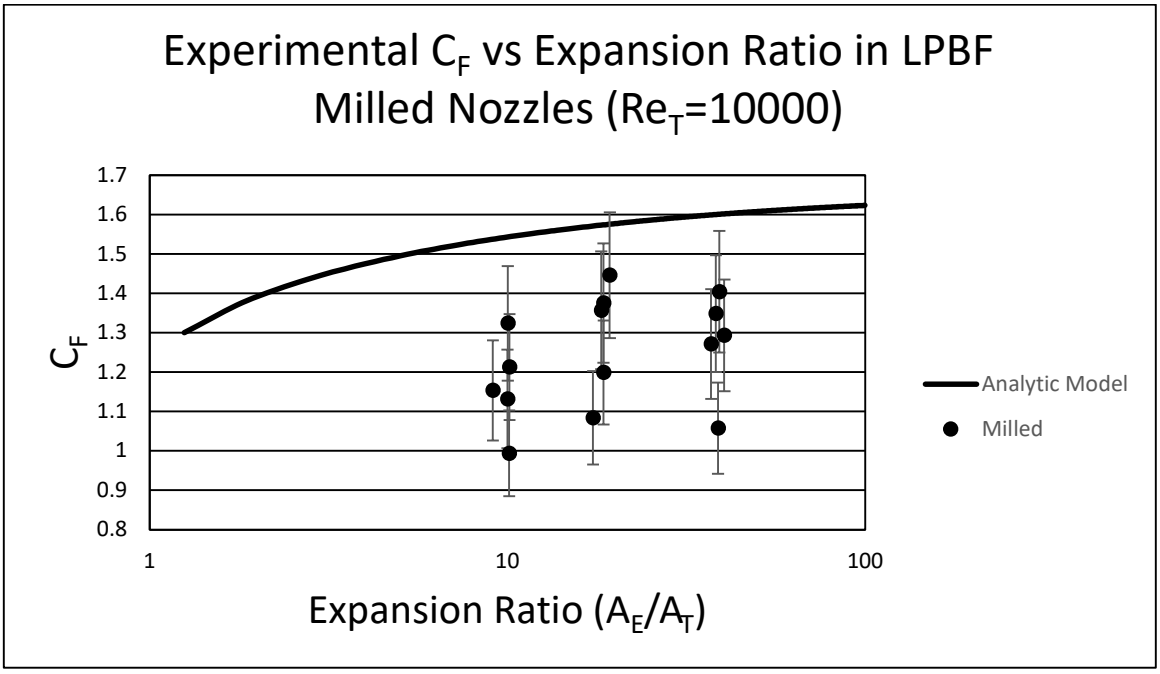

Figure 50: Thrust Coefficient vs Expansion Ratio in LPBF Milled Nozzles (Re=10000)

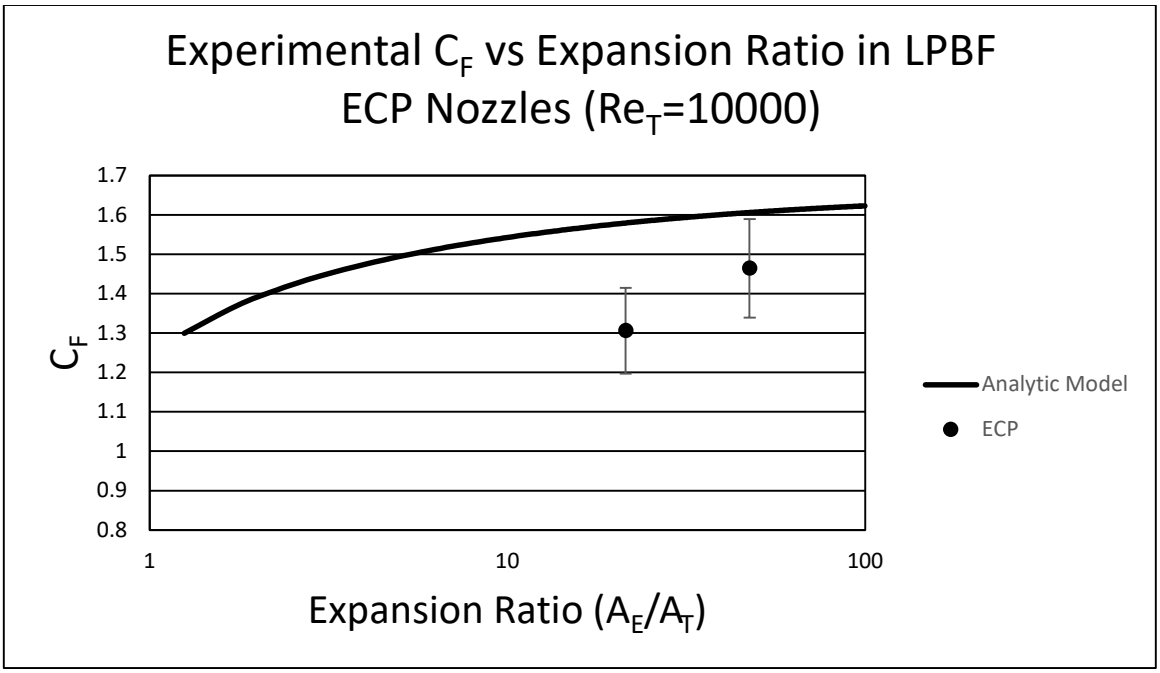

Figure 51: Thrust Coefficient vs Expansion Ratio in LPBF ECP Nozzles (Re=10000)

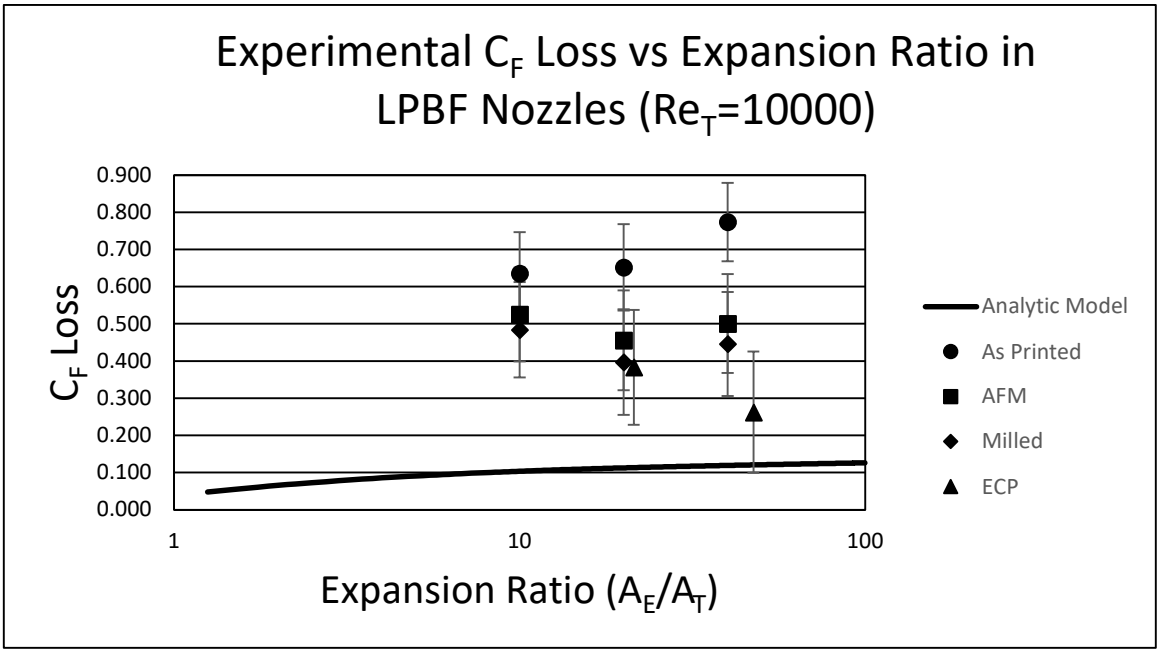

Figure 52: Thrust Coefficient Loss vs Expansion Ratio (Re=10000)

Bibliography

[1] F. Davoli, C. Kourogiorgas, M. Marchese, A. Panagopoulos and F. Patrone, "Small satellites and CubeSats: Survey of structures, architectures, and protocols," *John Wiley & Sons, Ltd.,* pp. 343-359, 2018.

[2] D. F. Everett, J. J. Puschell and J. R. Wertz, Space Mission Engineering: The New SMAD, Hawthorne: Microcosm Press, 2011.

[3] C. D. Tommila, "Performance losses in additively manufactured low thrust nozzles," M.S. thesis, Dept. of Aeronautics and Astronautics, Air Force Institute of Technology, 2017.

[4] C. R. Hartsfield, J. R. Komives, J. J. Redmond, T. E. Shelton and C. D. and Tommila, "Performance Impacts of Metal Additive Manufacturing of Very Small Nozzles," *Journal of aerospace engineering, ASCE,* 2021.

[5] E. W. Spisz et al., "Thrust coefficients of low-thrust nozzles," NASA, Cleveland, OH, TN D-3056,1965.

[6] G. P. Sutton and O. Biblarz, Rocket Propulsion Elements, 8th ed., Hoboken, NJ: John Wiley and Sons, Inc., 2010.

[7] S. P. Grisnik et al., "Experimental study of low Reynolds number nozzles," NASA, Cleveland, OH, NASA-TM-89858, 1987.

[8] M. V. Whalen, "Low Reynolds number nozzle flow study," NASA, Cleveland, OH, NASA-TM-100130, 1987.

[9] J. D. Anderson, Fundamentals of Aerodynamics, 5th ed., New York: McGraw Hill Education, 2010.

[10] P. H. Oosthuizen and W. E. Carscallen, Introduction to compressible fluid flow, Boca Raton, FL: Taylor and Francis Group, LLC, 2014.

[11] T. Adams, C. Grant and H. Watson, "A simple algorithm to relate measured surface roughness to equivalent sand-grain roughness," *International Journal of Mechanical Engineering and Mechatronics,* vol. 1, no. 1, pp. 66-71, 2012.

[12] C. R. Hartsfield, T. E. Shelton, G. R. Cobb, R. A. Kemnitz and J. Weber, "Understanding Flow Characteristics in Metal Additive Manufacturing," *Journal of Aerospace Engineering, ASCE,* 2021.

[13] V. S. Krishnamurty, et al., "Effect of wall roughness on the flow through converging-diverging nozzles," in *35th AIAA Aerospace Sciences Meeting and Exhibit* , Reno, NV, 1997.

[14] J. Portt, What is Wire EDM?, Ann Arbor, 1992.

[15] "Electrical Discharge Machining," [Online]. Available: https://www.sme.org/globalassets/sme.org/media/training-guides/dv03pub14_study_guide.pdf. [Accessed 4 September 2021].

[16] A. C. Petare and N. K. Jain, "A Critical Review of Past Research and Advances in Abrasive Flow Finishing Process," *The International Journal of Advanced Manufacturing Technology,* pp. 741-782, 2018.

[17] M. R. Munhoz, L. G. Dias, R. Breganon, F. S. F. Ribeiro, J. F. S. Goncalves, E. M. Hashimoto and C. E. S. Junior, "Analysis of the Surface Roughness Obtained by the Abrasive Flow Machining Process Using an Abrasive Paste with Oiticia Oil," *International Journal of Advanced Manufacturing Technology,* pp. 5061-5070, 2020.

[18] E. Uhlmann, C. Schmiedel and J. Wendler, "CFD Simulation of the Abrasive Flow Machining Process," *ScienceDirect,* pp. 209-214, 2015.

[19] G. Yang, B. Wang, K. Tawfiq, H. Wei, S. Zhou and G. Chen, "Electropolishing of Surfaces: Theory and Applications," *Taylor and Francis Group,* pp. 1-20, 2016.

[20] W. Schwartz, "Electropolishing," *Plating and Surface Finishing,* pp. 1-5, 2003.

[21] U. Ali, H. Fayazfar, F. Ahmed and E. Toyserkani, "Internal Surface Roughness Enhancement of Parts Made by Laser Powder-Bed Fusion Additive Manufacturing," *Science Direct,* pp. 1-5, 2020.

[22] S. Corporation, "Silcotek.com," [Online]. Available: https://www.silcotek.com/silcod-technologies. [Accessed 21 August 2021].

[23] L. Sun, Y. Guowen, L. Gao, J. Yang, M. Chhowalla, M. Gharahcheshmeh, K. Gleason, Y. Choi, B. Hong and Z. Liu, "Chemical Vapour Deposition," *Primer,* pp. 1-20, 2021.

[24] F. P. Incropera and D. P. DeWitt, Fundamentals of Heat and Mass Transfer, New York: J. Wiley, 2002.

[25] L. F. Moody, "Friction factors for pipe flow," *Transactions of the A.S.M.E,* vol. 66, pp. 671-677, 1944.

[26] Omega Engineering Inc., *FMA 5400/ FMA 5500 Mass Flow Controllers User's Guide,* Stamford, CT, 2001.

[27] Keyence, *Laser Scanning Microscope User Manual,* Japan, 2015.

[28] P. H. Oosthuizen and W. E. Carscallen, Compressible Fluid Flow, Graphics Press, 1997.

REPORT DOCUMENTATION PAGE

Form Approved
OMB No. 074-0188

1. REPORT DATE *(DD-MM-YYYY)*	2. REPORT TYPE	3. DATES COVERED *(From – To)*
03-06-2022	Master's Thesis	March 2021 – June 2022

TITLE AND SUBTITLE

PERFORMANCE STUDY OF POST-PROCESSED ADDITIVELY MANUFACTURED LOW THRUST NOZZLES

5a. CONTRACT NUMBER

5b. GRANT NUMBER

5c. PROGRAM ELEMENT NUMBER

6. AUTHOR(S)

Gerhold, Tyler W., Civilian, USAF

5d. PROJECT NUMBER

5e. TASK NUMBER

5f. WORK UNIT NUMBER

7. PERFORMING ORGANIZATION NAMES(S) AND ADDRESS(S)
Air Force Institute of Technology
Graduate School of Engineering and Management (AFIT/EN)
2950 Hobson Way, Building 640
WPAFB OH 45433-7765

8. PERFORMING ORGANIZATION REPORT NUMBER

AFIT-ENY-MS-22-J-074

9. SPONSORING/MONITORING AGENCY NAME(S) AND ADDRESS(ES)
Intentionally left blank

10. SPONSOR/MONITOR'S ACRONYM(S)

AFRL/RHIQ (example)

11. SPONSOR/MONITOR'S REPORT NUMBER(S)

12. DISTRIBUTION/AVAILABILITY STATEMENT
DISTRUBTION STATEMENT A. APPROVED FOR PUBLIC RELEASE; DISTRIBUTION UNLIMITED.

13. SUPPLEMENTARY NOTES

14. ABSTRACT
This research explores metal post-processing techniques to effectively reduce the large anomalous protrusions found in small additively manufactured low thrust rocket nozzles. Research has found that nozzles of this kind can experience losses in thrust of over 40%. Analytic theory of adiabatic nozzle flow with viscous losses for additively manufactured nozzles does not align with what has been found when tested experimentally. Compressible flow losses, such as shock wave formation inside the nozzle diverging cone, are likely the leading causes of such loss. Reduction in nozzle irregularities can likely yield results seen in analytic theory with similar performance to traditional subtractive manufacturing methods for low thrust nozzle design. Methods such as abrasive flow machining, electro-polishing, milling, wire EDM skimming, and high-temperature coatings are investigated and tested experimentally to compare laboratory results to analytic theory and traditionally manufactured low thrust nozzles. Nozzle performance increases showed to be greater than 20% across various explored post-processing techniques.

15. SUBJECT TERMS
Small satellite, additive manufacturing, low thrust, nozzle, metal post-processing, propulsion

16. SECURITY CLASSIFICATION OF:			17. LIMITATION OF ABSTRACT	18. NUMBER OF PAGES	19a. NAME OF RESPONSIBLE PERSON
a. REPORT	b. ABSTRACT	c. THIS PAGE			Dr. Carl Hartsfield, AFIT/ENY
U	U	U	UU	108	19b. TELEPHONE NUMBER *(Include area code)* (937) 785-3636, ext 4667 (carl.hartsfield@afit.edu)

Standard Form 298 (Rev. 8-98)
Prescribed by ANSI Std. Z39-18